Lithos 320–321 (2018) 515–536

Contents lists available at ScienceDirect

Lithos

journal homepage: www.elsevier.com/locate/lithos

A-type Medina batholith and post-collisional anatexis in the Araçuaí orogen (SE Brazil)

Paula Serrano [a,*], Antonio Pedrosa-Soares [a], Edgar Medeiros-Júnior [b], Tobias Fonte-Boa [a], Cristina Araujo [a], Ivo Dussin [c], Gláucia Queiroga [b], Cristiano Lana [b]

[a] Universidade Federal de Minas Gerais, Programa de Pós-Graduação em Geologia, CPMTC-IGC, Campus Pampulha, 31270-901 Belo Horizonte, Brazil
[b] Departamento de Geologia, Escola de Minas, Universidade Federal de Ouro Preto, Morro do Cruzeiro, R. Diogo de Vasconcelos, 122 Ouro Preto, Brazil
[c] Universidade do Estado do Rio de Janeiro, Faculdade de Geologia, R. São Francisco Xavier, 524 Rio de Janeiro, Brazil

ARTICLE INFO

Article history:
Received 21 February 2018
Accepted 9 September 2018
Available online 12 September 2018

Keywords:
Geochronology
Thermobarometry
A-type granites
Medina batholith
Araçuaí orogen

ABSTRACT

The Medina batholith and its host granitic migmatites record intriguing plutonic processes in the northern Araçuaí orogen (SE Brazil). This orogen shows a long lasting (630–480 Ma) succession of granite production events from the earliest pre-collisional plutons to the latest post-collisional intrusions. The Medina batholith includes granite intrusions ascribed to the post-collisional stage. They show high alkali and halogen contents, low CaO (at $SiO_2 = 71\%$: $Na_2O + K_2O = 7$ to 9%; CaO = 1.6%), and high $FeO_t/(FeO_t + MgO)$ ratios (0.78 to 0.92). The Medina granites are metaluminous to weakly peraluminous, with ASI (molecular ratio Al/(Ca-1.67P + Na_K)) values of 1.76 to 2.07, and have high concentrations of high field strength elements (Zr + Nb + Ce + Y > 700 ppm), as well as high Ga/Al ratios. Accordingly, the Medina intrusions are typical ferroan A-type granites. U—Pb ages from zircon (501 ± 2 Ma) and monazite (497 ± 2 Ma) constrain the emplacement timing of the Medina batholith. Surprisingly, all monazite ages from host rocks also cluster around 500 Ma, despite their nature and distance from the batholith, suggesting that they would have shared a same thermal process. The studied host rocks are granitic migmatites varying from patch metatexite to nebulitic diatexite, comprising paleosome of foliated sillimanite-garnet-biotite metagranite to gneiss, and non-foliated garnet-cordierite neosome poor to free of biotite. A metatexite (R14) located relatively far from the Medina batholith, and a diatexite (M26) found at the batholith contact were sampled for detailed studies. The paleosome of foliated metagranite (R14A) only shows zircon grains with igneous features and Th/U ratio from 1.64 to 0.26. Although the spreading of zircon spots, the main cluster yields a Concordia age at 556 ± 6 Ma, constraining the protolith magmatic crystallization. A minor cluster furnishes a Concordia age at 499 ± 7 Ma, in agreement with the U—Pb monazite age at 501 ± 2 Ma. Extracted from the same metatexite sample, the non-foliated garnet-cordierite neosome (R14B) shows both igneous and metamorphic zircon domains with Th/U ratios ranging from 1.47 to 0.00. Again, the U—Pb spots cluster at two distinct Concordia ages (562 ± 3 Ma and 499 ± 3 Ma). The youngest of them, fitting with the monazite age (495 ± 3 Ma), constrains melt crystallization, while the oldest age suggests paleosome inheritance. The nebulitic diatexite (M26) shows monazite (497 ± 2 Ma) and zircon (Th/U = 1.7 to 0.0; Concordia ages at 564 ± 2 Ma and 507 ± 3 Ma) populations similar to the metatexite neosome, also with the youngest ages bracketing the melt crystallization process around 500 Ma. Accordingly, all those ages at around 500 Ma disclose a partial melting episode coeval with the Medina batholith emplacement. Phase equilibrium modeling on a garnet-cordierite neosome furnished P-T conditions of 750–840 °C at 2.4–3.5 kbar for that post-collisional anatexis. Evidence for such a late thermal event are common in the Araçuaí orogen, even far from the post-collisional batholiths. Thus, a possible major heat source can be envisaged, like a mantle plume triggering crustal anatexis and regional fluid circulation during the gravitational collapse of the Araçuaí orogen.

1. Introduction

A-type granites define a particular group within the granite set. They are relatively potassic, iron and HFSE enriched, and crystallized from high temperature melts (Eby, 1990; Frost and Frost, 1997; Loiselle and Wones, 1979; Whalen et al., 1987). High mantle heat flow or involvement of mafic magmas is required to justify such high temperatures in

* Corresponding author at: Universidade Federal de Minas Gerais, Programa de Pos-Graduação em Geologia, CPMTC-IGC, Av. Antônio Carlos, 6627 Belo Horizonte, Brazil.
E-mail address: pms@ufmg.br (P. Serrano).

https://doi.org/10.1016/j.lithos.2018.09.009
0024-4937/

the source regions. According to Eby (1990, 1992), the A-type granites can be chemically divided into two groups, A1 and A2. Primeval sources of the A1 group can be related to those of the oceanic-island basalts, whereas the A2 group has also certain relations to average continental crust.

The Araçuaí orogen was the scene of a long and fascinating history of abundant granite production (Fig. 1), especially if we take into account its confined nature because it developed within an embayment largely surrounded by cratonic landmasses (Alkmim et al., 2006, 2017; Pedrosa-Soares et al., 2001, 2008, 2011). Voluminous granitic rocks with distinct signatures formed during a long time span (630–480 Ma; Table 1), representing pre-collisional, collisional and post-collisional tectonic stages, occur in southern and northern sectors of the Araçuaí orogen (Pedrosa-Soares et al., 2011). The southern sector shows ophiolite slivers and a calc-alkalic magmatic arc, testifying oceanic spreading and subduction, whereas the northern segment evolved in an ensialic setting (Gonçalves et al., 2016; Pedrosa-Soares et al., 2001, 2008). Therefore, models based on ocean-floor subduction, continental collision, and post-collisional processes involving gravitational collapse, asthenosphere upwelling and hot spot rising are reliable to explain all granite production events in the southern sector of the orogen (De Campos et al., 2016; Gradim et al., 2014; Tedeschi et al., 2016), where

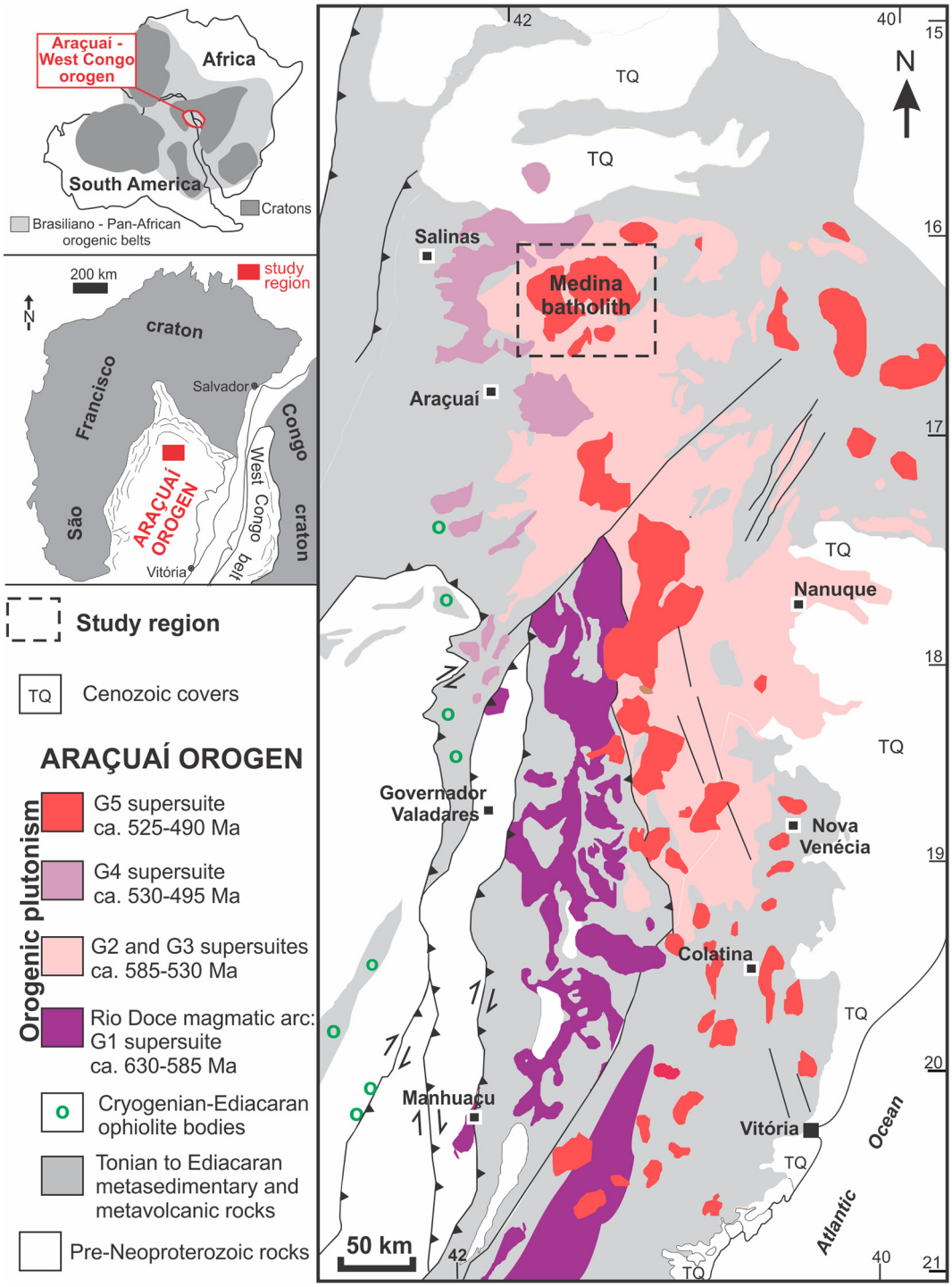

Fig. 1. Geotectonic setting and geological map of the Araçuaí orogen, showing the location of the study region (modified from Pedrosa-Soares et al., 2011).

Table 1
Main characteristics of the G1 to G5 granitic supersuites of the Araçuaí orogen, based on data from Medeiros et al. (2000), de Martins et al. (2004), Pedrosa-Soares et al. (2011), Belém (2014), Gradim et al. (2014), Gonçalves et al. (2016), De Campos et al. (2016), Tedeschi et al. (2016), Melo et al. (2017a,b), Deluca et al. (2018), and the present paper.

Supersuite	G1	G2	G3	G4	G5
U-Pb age (Ma)	630–580	585–540	545–500	530–490	525–480
Lithotypes	Mostly tonalite to granodiorite, minor diorite to gabbronorite, with biotite, amphibole and/or pyroxenes	Mostly biotite-garnet syenogranite to alkali feldspar granite, minor monzogranite to tonalite rich in garnet, and garnet-two-mica granite, locally with sillimanite	Alkali feldspar granite to syenogranite with cordierite and/or garnet, poor to free of biotite	Two-mica granite generally with garnet, pegmatoid granite, and minor biotite granite	Alkali feldspar granite to granodiorite, and corresponding Opx-bearing (charnockitic) rocks, minor enderbite and norite
Field relations	Batholiths and stocks, generally rich in intermediate to mafic enclaves, showing solid-state deformation and migmatization, local well-preserved igneous fabrics, associated with the arc-related metavolcano-sedimentary Rio Doce Group	Batholiths, stocks and stratoid bodies, showing solid-state deformation, metamorphism and migmatization, local well-preserved igneous fabrics, with common restites and xenoliths of metasedimentary rocks	Non-deformed patches, veins and lodes, and minor stocks, free of the regional foliation, hosted by migmatites with G2 paleosome	Intrusive, balloon-shaped plutons, minor stratoid bodies, generally free of the regional deformation	Intrusive, balloon-shaped plutons, batholiths, free of the regional solid state deformation, rich in magma mingling and mixture features, with mafic to intermediate enclaves
Lithochemistry	Metaluminous to slight peraluminous, magnesian, calcic to alkali-calcic, medium- to high-K, expanded calc-alkaline series	Peraluminous, calc-alkalic to sub-alkalic	Peraluminous, sub-alkalic to high-K alkalic	Peraluminous, sub-alkalic (K > Na) to alkalic (Na > K)	Metaluminous to slightly peraluminous, high K—Fe calc-alkaline to alkaline, minor tholeiite
Isotopic signature	Whole-rock $\varepsilon Nd_{(t)}$: −4 to −13	Whole-rock $\varepsilon Nd_{(t)}$: −5 to −13	$\varepsilon Hf_{(t)}$ in zircon: −4 to −10	$^{87}Sr/^{86}Sr_{(i)}$: 0.713	Whole-rock $\varepsilon Nd_{(t)}$: −6 to −23
	Nd TDM ages: 1.2 to 1.8 Ga	Nd TDM ages: 1.3 to 1.9 Ga	Hf TDM ages: 1.3 to 1.7 Ga		Nd TDM ages: 1.4 to 2.5 Ga
	Whole-rock $^{87}Sr/^{86}Sr_{(i)}$: 0.704 to 0.711	Whole-rock $^{87}Sr/^{86}Sr_{(i)}$: 0.707 to 0.713			$^{87}Sr/^{86}Sr_{(t)}$: 0.702 to 0.716
	$\varepsilon Hf_{(t)}$ in zircon: −3 to −15	$\varepsilon Hf_{(t)}$ in zircon: −2 to −8			
	Hf TDM ages: 1.3 to 1.7 Ga	Hf TDM ages: 1.3 to 1.9 Ga			
Genetic type	Mostly metaluminous I-type, minor peraluminous I-type	Mostly S-type, minor peraluminous I-type	S-type	S-type	A-type and I-type
Tectonic stage and setting	Pre-collisional to early collisional, continental margin magmatic arc (Rio Doce arc)	Late pre-collisional to late collisional	Late collisional to post-collisional	Late collisional to post-collisional	Post-collisional

a complete Wilson cycle took place (Alkmim et al., 2006, 2017). However, those models generally become ineffective or lack data support to explain the abundant collisional and post-collisional granites emplaced in the ensialic sector of the Araçuaí orogen (Pedrosa-Soares et al., 2011).

The aim of this paper is to study a large plutonic mass mostly comprising A-type granites, the Medina batholith (~1000 km^2), emplaced in the ensialic sector of the Araçuaí orogen, and its potential relation with intriguing melting processes shown by the host rocks (Figs. 1 and 2). For that, we present many new data, and discuss the available petrographic, lithochemical and geochronological dataset from Medina granites and their host rocks, in the light of their field relations and tectonic setting. Furthermore, aiming a better knowledge of the P-T conditions on host rocks, we built pseudosections for samples with zircon and monazite U—Pb ages. Ultimately, all those data, together with evidence from literature, allow us to suggest a mantle plume as a potential major heat supplier for post-collisional anatexis in the northern Araçuaí orogen.

2. Geological setting

The Neoproterozoic Araçuaí - West Congo orogenic system (AWCO) developed during the assembly of West Gondwana, as part of the Neoproterozoic-Cambrian Brasiliano – Pan-African belts that once linked terranes now located in southeastern Brazil and southwestern Africa. At the time it formed, the AWCO's precursor basin was like a big gulf largely surrounded by cratonic land of the São Francisco-Congo paleocontinent, but partially floored by ocean crust (Alkmim et al., 2006, 2017; Pedrosa-Soares et al., 1998, 2001, 2008). That gulf was connected to an ocean, the Adamastor ocean, which closure resulted in the amalgamation of the central West Gondwana (Cordani et al., 2003). Owing to the nature of its precursor basin, the AWCO was shaped like a confined orogenic system within an embayment of the São Francisco-Congo craton. That orogenic system was split apart in the Cretaceous by the opening of the South Atlantic Ocean. The Brazilian counterpart, called Araçuaí orogen, inherited two thirds of the AWCO, comprising a sector with ophiolite bodies and a magmatic arc, to the south, and an ensialic sector to the north (Alkmim et al., 2017; Pedrosa-Soares et al., 2001, 2008).

One of the most remarkable features of the Araçuaí orogen is a long history of granite production events (630–480 Ma), from the beginning of magmatic activity in the Rio Doce magmatic arc to the last post-collisional intrusions (De Campos et al., 2016; Gradim et al., 2014; Melo et al., 2017a,b; Pedrosa-Soares et al., 2011; Tedeschi et al., 2016). Around one third of the orogenic region consists of granitic rocks, and related gneisses and granulites. Based on field relations, structural features, geochemical, geochronological and isotopic data (Table 1), those rocks (s.l.) have been grouped into five supersuites (*cf.* Pedrosa-Soares et al., 2011), named: G1 (pre-collisional, c. 630–580 Ma), G2 (*syn*-collisional, c. 585–540 Ma), G3 (late collisional to post-collisional, c. 545–500 Ma), G4 (late collisional to post-collisional, c. 530–490 Ma) and G5 (post-collisional, c. 530–480 Ma). This paper focuses on rocks of the G2, G3 and G5 supersuites to reveal their field relations.

Despite assigned to distinct tectonic stages of the Araçuaí orogen development, those supersuites can show age overlaps owing to transitions in time and space from one stage to another along distinct regions of the orogen (Pedrosa-Soares et al., 2011; Gradim et al., 2014; Peixoto et al., 2015, 2018; Gonçalves-Dias et al., 2016; Richter et al., 2016). The G1 supersuite (Fig. 1, Table 1), developed from the pre-collisional to early collisional stages of the Araçuaí orogen, represents the plutonic part of the Rio Doce magmatic arc (Gonçalves et al., 2016, 2018; Narduzzi et al., 2017; Novo et al., 2018; Tedeschi et al., 2016).

The collisional stage was accompanied by regional deformation and metamorphism, imposing anatectic processes on peraluminous gneisses under high - T amphibolite to granulite facies conditions (Degler et al., 2017; Gonçalves-Dias et al., 2016; Gradim et al., 2014; Richter et al., 2016). Those paragneisses were responsible for the generation of a large amount of peraluminous biotite-garnet and garnet-two-mica granites grouped in the G2 supersuite (Pedrosa-Soares et al., 2011). These rocks are especially abundant in the back-arc zone (Gradim et al., 2014; Melo et al., 2017a,b) and northern region (Gonçalves-Dias et al., 2016; Paes et al., 2010) of the Araçuaí orogen (Fig. 1; Table 1). The G2 granitic bodies generally show solid-state deformation and related metamorphism to anatexis, displaying a prominent regional foliation, although well-preserved igneous features can be locally found within batholiths and stocks. Actually, the G2 supersuite mostly occurs in migmatitic massifs, comprising paleosomes composed by foliated G2 metagranite to gneiss, and neosomes consisting of non-foliated G3 granites (Pedrosa-Soares et al., 2011).

Following the collisional stage, the fading of convergent stresses together with crustal overthickening assisted the gravitational collapse of the orogenic building under extension and decompression, triggering late collisional to post-collisional igneous activities. During that tectonic phase were formed the G3, G4 and G5 supersuites, representing different plutonic assemblages related to distinct petrogenetic processes (Table 1).

The G3 supersuite mostly includes patches, veins and lodes, and minor stocks, composed by non-foliated garnet-cordierite migmatites poor to free of biotite, which are post-kinematic to the regional foliation imprinted in their host rocks. They generally occur in close association with the G2 supersuite, both forming migmatitic massifs comprising neosomes of G3 granite and paleosomes of G2 metagranite to gneiss. The G3 granite neosomes usually show gradational contacts in relation to the host G2 rocks, suggesting the G3 melts have formed from autochthonous partial melting of G2 metagranites (Gradim et al., 2014; Pedrosa-Soares et al., 2011).

Partial melting of metasedimentary rocks in relatively shallow crustal levels formed the two-mica leucogranites of the G4 supersuite, while anatectic processes in the deep crust rich in meta-igneous rocks originated a myriad of intrusions grouped in the G5 supersuite (Pedrosa-Soares et al., 2011). The G5 supersuite mostly includes I-type and A-type granitic rocks, and their Opx-bearing charnockitic equivalents, generally with significant amounts of melanocratic to mesocratic microgranular enclaves (Table 1). In the southern Araçuaí orogen (Fig. 1), G5 intrusions usually form inversely-zoned balloon-like plutons, composed of granitic-charnockitic rocks and gabbronoritic cores, with striking magma mixing and mingling features, and chemical-isotopic evidence of mantle involvement in G5 granite genesis (De Campos et al., 2004, 2016). To the north, where relatively upper crustal levels are exposed, amalgamated G5 intrusions make up granitic-charnockitic batholiths with much less mafic components (Pedrosa-Soares et al., 2011). Among them, the Medina batholith is one of the largest granite assemblage of the G5 supersuite (Fig. 1).

Such a long-lasting history (630–480 Ma) of granite production events, related to different tectonic stages of an orogenic evolution, definitely requires distinct heat sources and catalyzing melting processes. Published models have evoked ocean-floor subduction and pre-collisional ascent of mantle magma, thrusting of the hot arc over fertile metasedimentary piles, collisional crustal overthickening, asthenosphere upwelling accompanying slab break-off and delamination of lithospheric mantle, and post-collisional hot spots (De Campos et al., 2016; Gonçalves et al., 2016; Gradim et al., 2014; Pedrosa-Soares et al., 2001, 2011; Tedeschi et al., 2016).

3. The Medina granites and host rocks

Large areas covered by collisional to post-collisional granitic rocks characterize the ensialic sector of the Araçuaí orogen (Fig. 1), where the Medina batholith is the largest post-collisional G5 plutonic assemblage (Fig. 2). The batholith consists of granite intrusions mainly hosted

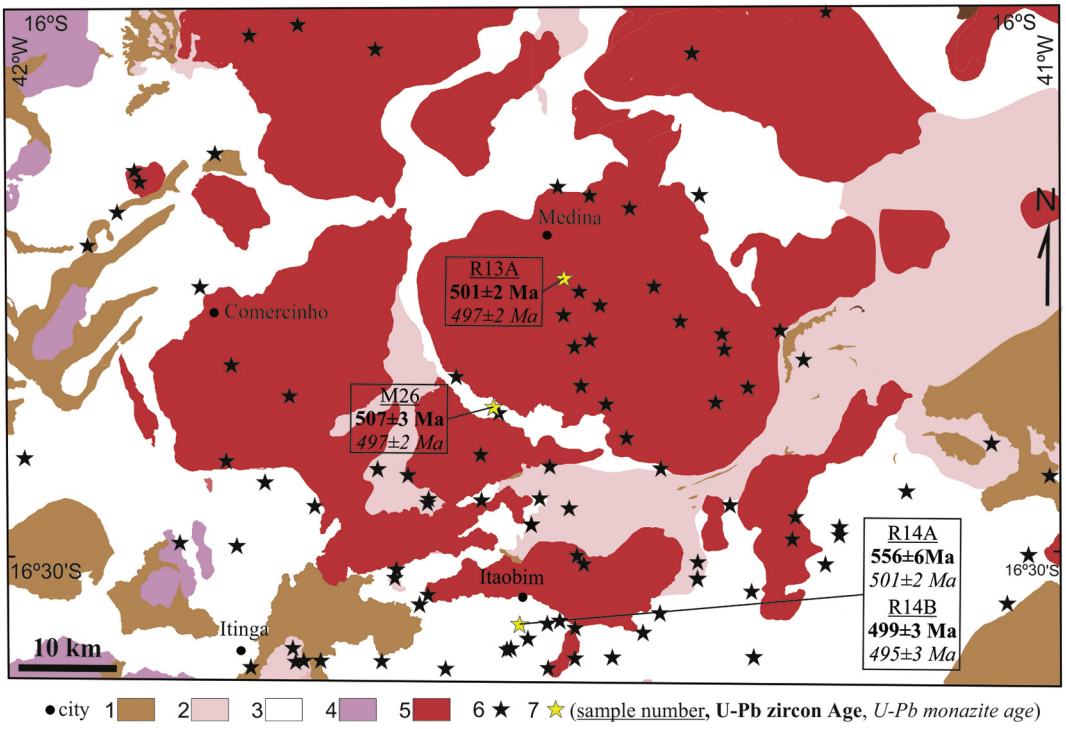

Fig. 2. Simplified geological map of Medina batholith and its host rocks (modified from Paes et al., 2010). 1, Neoproterozoic metasedimentary units; 2, G2 metagranite to gneiss and minor metatexite; 3, Metatexite to diatexite with paleosome composed of G2 metagranite to gneiss, and neosome consisting of non-foliated G3 granite; 4, G4 granites; 5, G5 biotite granites (Medina batholith); 6, samples for lithochemical analysis; 7, samples for zircon and monazite U—Pb analysis and geothermobarometric studies.

by granitic migmatites with paleosome composed of G2 metagranite to gneiss, and non-foliated G3 neosome (Fig. 2).

This paper presents analytical data from microprobe mineral chemistry, lithochemistry, and isotopic geochronology of zircon and monazite, as well as calculations of pressure and temperature (P-T) conditions for rock crystallization. Descriptions of the analytical methods, laboratory conditions, references to analytical standards, as well as the data tables are available in the Supplementary Data Files.

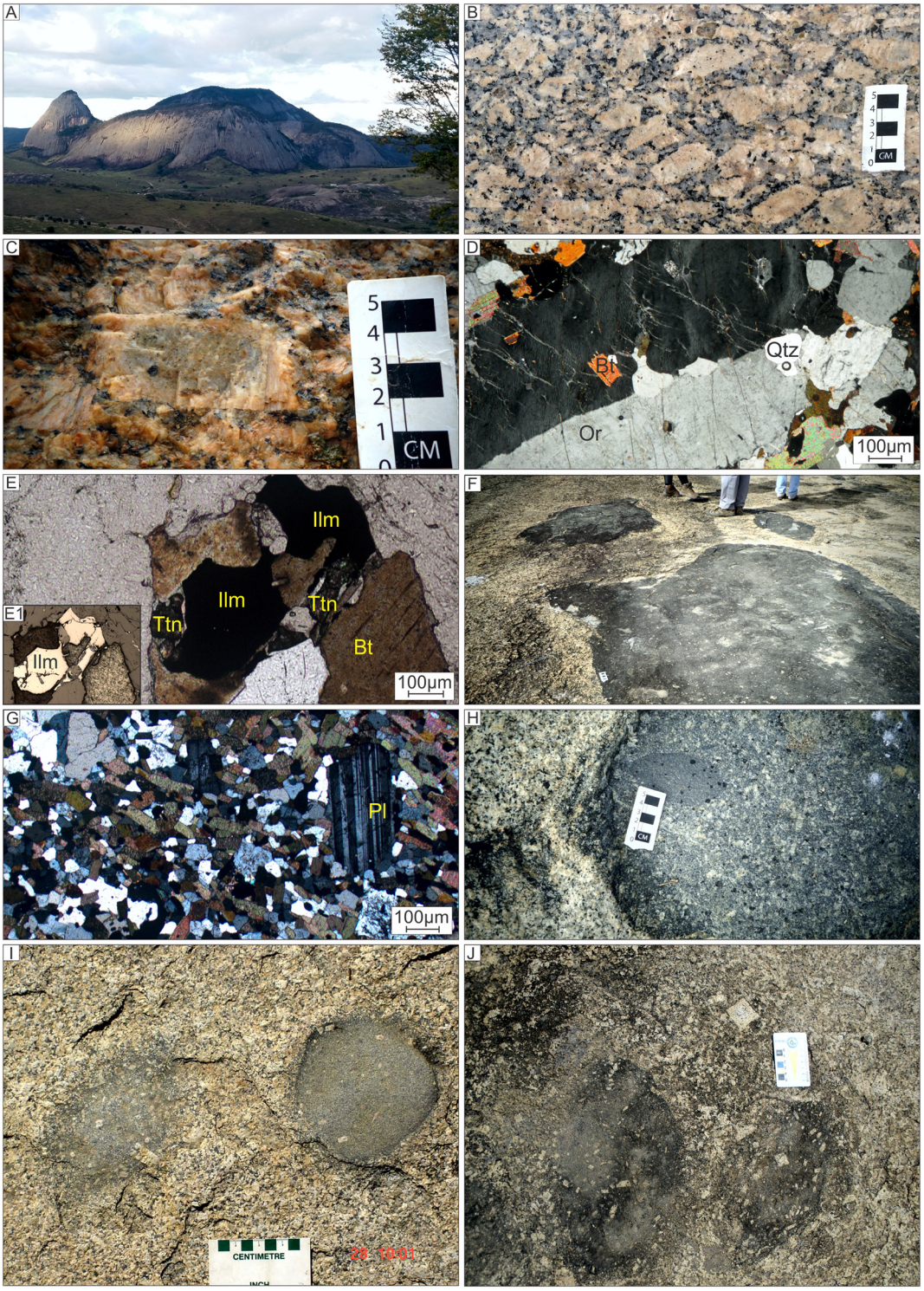

Fig. 3. The Medina batholith: (A) sugarloaf landform on granite; (B) coarse-grained biotite monzogranite rich in feldspar megacrysts, showing weak igneous flow, and rapakivi and anti-rapakivi textures; (C) euhedral feldspar megacryst with anti-rapakivi texture, within the coarse-grained granitic matrix; (D) photomicrography (crossed polarizers) from a granite, showing a corroded phenocryst of micropertithic ortoclase with Carlsbad twinning, and inclusions of quartz and biotite; (E) photomicrography (parallel polarizers) of a granite, highlighting accessory ilmenite (Ilm) and titanite (Ttn); (F) large enclaves surrounded and cut by granite rich in feldspar clusters; (G) photomicrography (crossed polarizers) from an enclave, showing plagioclase (Pl) within a matrix rich in biotite and quartz; (H) enclave rich in feldspar xenocrysts, showing a more mafic finer-grained residue (melanocratic elliptical body near the scale); (I) coarse-grained granite showing a rounded dark-gray enclave with biotite-rich rims (chilled margin) poor in feldspar xenocrysts, and a roughly elliptical light-gray enclave rich in feldspar xenocrysts displaying diffuse contact with the host granite, and a feldspar xenocryst "frozen" when cutting across the enclave-granite contact; (J) melanocratic enclaves rich in feldspar xenocrysts locally outlining igneous flow.

Table 2
Representative composition of alkali feldspar.

Supersuite	G5				G2				G3							
Sample	R13A				R14A				R14B				M26			
	Afs				Afs				Afs				Afs			
Analysis number	4 core	2SD[a]	4 rim	2SD	8 core	2SD	6 rim	2SD	5 core	2SD	3 rim	2SD	6 core	2SD	5 rim	2SD
wt%																
SiO_2	64.68	0.25	64.48	0.53	64.48	0.48	64.47	0.89	64.62	0.68	64.20	1.78	64.57	1.54	64.74	0.39
Al_2O_3	18.63	0.25	18.73	0.10	18.76	0.38	18.85	0.30	18.70	0.42	19.07	1.01	18.88	0.20	18.98	0.38
BaO	0.30	0.00	0.35	0.12	0.21	0.07	0.20	0.00	0.20	0.00	0.20	0.00	0.10	0.00	0.10	0.00
CaO	0.03	0.10	0.00	0.00	0.04	0.10	0.03	0.10	0.06	0.11	0.10	0.00	0.15	0.24	0.18	0.17
Na_2O	1.35	0.20	1.40	0.16	1.49	0.47	1.47	0.69	1.34	0.18	1.47	0.61	2.20	1.66	2.18	1.58
K_2O	15.25	0.26	15.15	0.12	14.78	0.81	14.88	1.43	14.94	0.41	14.73	1.10	13.85	2.44	13.84	2.20
Total	100.28	0.30	100.08	0.41	99.74	0.93	99.90	1.62	99.78	1.05	99.77	0.81	99.68	1.50	99.98	0.61
% molar																
Ab	11.98	1.38	12.25	0.74	13.10	4.28	12.92	6.75	11.90	1.83	13.27	5.46	19.15	14.41	19.12	13.47
An	0.20	0.28	0.08	1.10	0.24	0.18	0.18	0.08	0.26	0.11	0.20	0.35	0.72	0.92	0.82	1.02
Or	87.83	1.64	87.63	0.82	86.66	4.31	86.88	6.80	87.82	1.89	86.57	5.61	80.12	15.19	80.08	14.31

[a] 2SD = 2 Standard deviation.

3.1. Medina granites

The Medina batholith comprises an assemblage of biotite granites that strikingly differ from their host rocks, which are peraluminous granitic migmatites and migmatitic paragneisses (Fernandes, 1991; Paes et al., 2010; Pedrosa-Soares and Wiedemann-Leonardos, 2000). Formerly only considered as I-type granites of the post-collisional G5 suite of the Araçuaí orogen (Pedrosa-Soares et al., 2001; Pedrosa-Soares and Wiedemann-Leonardos, 2000), some Medina granites were reclassified as A2-type granites (Paes et al., 2010). After that, the Medina batholith was included in the redefined G5 supersuite (Pedrosa-Soares et al., 2011), together with many other post-collisional I- and A-type intrusions found in the Araçuaí orogen (Table 1). The Medina batholith encompasses a set of G5 granite intrusions, emerging as a composite elliptical body with around 38 km E-W and 27 km N-S (Fig. 2). Its surface area over 1000 km^2 shows superb sugarloaf landforms shaped on granite intrusions (Fig. 3A).

The main composition of the studied Medina granites ranges from biotite-bearing syenogranite to monzogranite (Fig. 3B, C and D). Common accessory minerals are titanite, allanite, ilmenite, magnetite, apatite, monazite and zircon (Fig. 3E). Muscovite, epidote, carbonate, sericite and chlorite are minerals from late alteration processes. Biotite is the main mafic phase and reaches modal values of 10%. The granites generally display coarse- to medium-grained, inequigranular to porphyritic textures with variable amounts of euhedral to subhedral (roughly rectangular) and anhedral (rapakivi-like ovoid), K-feldspar phenocrysts (3–10 cm) (Fig. 3B, C and D). K-feldspar varies from dominant microcline to minor orthoclase, and sometimes it show compositional zoning revealed by distinct colors (light gray, pink, light yellow or cream) from core to rim (Fig. 3C). They show corroded features by matrix minerals, indicating crystallization during early magmatic stage (Fig. 3D).

The Medina granites often show mesocratic to melanocratic microgranular enclaves with variable sizes, from centimeters to meters, and shapes, from bubble-like and egg-shaped to irregular bodies with sharp angle edges (Fig. 3F, H, I, and J). They are essentially composed of plagioclase, biotite, quartz and hornblende, generally with a tonalitic composition (Fig. 3G). The enclave-granite contacts are usually abrupt and marked by thin rims enriched in mafic minerals, resembling chilled margins of originally hotter enclaves within the relatively colder granite magma (Fig. 3F, H, and I). K-feldspar xenocrysts are common within the enclaves (Fig. 3H, I and J). They can outline distinct igneous flow within the enclave, but discordant of the flow orientation shown by the host granite (Fig. 3H and J). Feldspar phenocrysts "frozen" in the way to cut across the enclave-granite contact, as well as concentrated outside the biotite-rich enclave rims are common (Fig. 3F, H and J). All these enclave features are evidence of magma mingling processes. In some points, however, the contact between the enclave and host granite tends to be diffuse, owing to the gradual enrichment of felsic minerals from the granite inward the enclave (Fig. 3H, I and J), suggesting gradual mixing between their parental magmas (Fernandes, 1991).

Table 3
Representative composition of plagioclase.

Supersuite	G5								G2				G3							
Sample	R13A				R13E				R14A				R14B				M26			
	Pl				Pl				Pl				Pl				Pl			
Analysis number	19 core	2SD[a]	8 rim	2SD	25 core	2SD	12 rim	2SD	9 core	2SD	6 rim	2SD	10 core	2SD	7 rim	2SD	12 core	2SD	11 rim	2SD
wt%																				
SiO_2	64.65	1.67	64.70	0.89	63.44	1.53	63.64	1.15	64.18	0.61	64.03	0.50	63.84	0.80	64.46	2.99	64.10	0.75	63.95	1.06
Al_2O_3	23.19	1.91	23.15	1.74	24.77	2.13	24.58	1.55	22.27	0.45	22.40	0.59	22.52	0.28	21.97	1.53	22.28	0.47	22.28	0.23
BaO	0.00	0.00	0.00	0.00	0.00	0.00	0.00	0.00	0.00	0.00	0.00	0.00	0.00	0.00	0.00	0.00	0.00	0.00	0.00	0.00
CaO	2.93	1.73	2.89	1.61	3.56	1.24	3.28	1.05	3.17	0.42	3.22	0.27	3.27	0.31	2.76	1.68	3.04	0.20	3.02	0.55
Na_2O	8.72	1.69	8.83	1.70	7.95	1.48	8.14	0.82	9.64	0.27	9.58	0.27	9.52	0.25	9.53	0.28	9.66	0.29	9.70	0.36
K_2O	0.25	0.15	0.24	0.15	0.19	0.56	0.17	0.23	0.27	0.10	0.25	0.17	0.38	0.16	0.33	0.10	0.33	0.19	0.29	0.14
Total	99.80	0.91	99.78	1.68	99.90	1.30	99.81	1.14	99.48	0.84	99.45	0.75	99.50	0.81	99.04	1.08	99.42	0.73	99.24	0.69
% molar																				
Ab	82.78	10.15	83.41	9.49	79.09	9.26	80.83	5.62	83.38	1.74	83.23	1.74	82.13	1.36	82.74	2.55	83.58	1.34	83.97	2.89
An	15.58	9.44	15.13	8.88	19.71	8.36	18.00	6.24	15.17	1.98	15.37	1.07	15.72	1.21	15.39	2.12	14.57	0.83	14.45	2.55
Or	1.65	1.01	1.44	0.83	1.19	3.48	1.17	1.54	1.48	0.46	1.37	0.89	2.15	0.90	1.84	0.55	1.86	0.96	1.59	0.93

[a] 2SD = 2 Standard deviation.

3.2. Mineral chemistry of Medina batholith

The results of complete electron microprobe analyses of K-feldspar, plagioclase and biotite are listed in Tables 2 to 4.

Representative K-feldspar compositions range from Or_{86} to Or_{88}. Plagioclase varies from albite (An_2) to oligoclase (An_{21}). Feldspars often show rapakivi and anti-rapakivi textures (Fig. 3B and C).

Biotite of the Medina granites has high siderophyllite-annite contents with $Fe^{2+}/(Fe^{2+}+Mg)$ ranging from 0.72 to 0.75, Al^{IV} from 2.5 to 2.6 a.p.f.u. and TiO_2 from 2.27 to 2.75 wt% (sample R13A, Table 4). The biotite of enclave has $Fe^{2+}/(Fe^{2+}+Mg)$ ranging from 0.73 to 0.76, Al^{IV} from 2.4 to 2.6 a.p.f.u. and TiO_2 from 1.73 to 2.64 wt% (sample R13E, Table 4). All biotite in both types have high contents of F (mean = 1.54, 2SD = 0.17 wt% for Medina granites; mean = 1.93, 2SD = 0.21 wt% for enclave) and Cl (mean = 0.51, 2SD = 0.10 wt% for Medina granites; mean = 0.50, 2SD = 0.04 wt% for enclave) (Table 4).

3.3. Studied host rocks

The focused host rocks of the Medina batholith are migmatites (Figs. 2 and 4), varying from patch metatexite (Fig. 4A and B) to nebulitic diatexite (Fig. 4E and F). They consist of variable amounts of paleosome composed of G2 metagranite to gneiss, and non-foliated G3 garnet-cordierite neosome.

The studied metatexite (R14) consists of scattered patches of leucocratic non-foliated garnet-cordierite neosome, hosted by a dominant mesocratic paleosome consisting of foliated sillimanite-garnet-biotite metagranite (Fig. 4A). Along the outcrop, the paleosome varies from weakly foliated to striped gneissic structure (Fig. 4B). The paleosome is a fine- to medium-grained, foliated, sillimanite-garnet-biotite metagranite (Fig. 4C), very similar to many others regionally ascribed to the G2 supersuite (*cf.* Gradim et al., 2014; Pedrosa-Soares et al., 2011; Richter et al., 2016). Biotite and garnet are the main mafic phases, reaching modal values around 10–15% and 5–10%, respectively. The paleosome composition ranges from monzogranitic to syenogranitic, with sillimanite, hercynite, apatite, monazite, zircon, ilmenite and rutile as accessory minerals. The orientation of biotite flakes, sillimanite fibers to needles, and stretched quartz and feldspars materializes the regional solid-state foliation within the granitic paleosome, in concordance with the foliation of the country metasedimentary rocks. This foliation can be ascribed to the regional Barrovian-type metamorphism related to the collisional climax at around 575–550 Ma (Pedrosa-Soares et al., 2011; Peixoto et al., 2018). The neosome consists of leucocratic irregular-shaped patches and minor veins, which are easily recognized in outcrop owing to coarser grain-size and isotropic structure contrasting with the finer-grained foliated paleosome (Fig. 4A and B). There are no rims of melanosome around the neosome, which shows prominent cordierite clusters surrounded by quartz-feldspathic matrix (Fig. 4A and B). The neosome mineral assemblage essentially includes quartz, perthitic K-feldspar and minor free plagioclase (oligoclase). Cordierite, garnet, apatite, zircon, monazite, and very scarce biotite and opaque minerals are accessory minerals. Cordierite shows variable degrees of pinitization (Fig. 4D). The scarce biotite can be related to alteration processes and/or relics from the anatectic process. Although the neosome patches and veins clearly overprint prior structures, they show grading and diffuse contacts with the paleosome, suggesting autochthonous partial melting (Fig. 4A and B). This feature also suggests that the melting process mostly involved consumption of biotite from the paleosome. Cordierite is, thus, a neoformed peritectic mineral in the R14 metatexite neosome, as that phase is absent from the paleosome mineral assemblage (Fig. 4A, B and D).

The studied diatexite M26 resembles a nebulitic migmatite mostly composed by isotropic garnet-cordierite neosome, and very minor paleosome of foliated sillimanite-garnet-biotite metagranite (Fig. 4E and F). The neosome is a porphyritic garnet-cordierite syenogranite

Table 4
Representative composition of biotite, garnet and cordierite.

Supersuite	G2		G3			G5			G5			G2			G3				G3					
Sample	R14A		R14B		M26	R13A		R13E				R14A			M26				M26					
	Bt		Bt		Bt	Bt		Bt				Grt			Grt				Crd					
Analysis number	$n = 23$	2SD[a]	$n = 23$	2SD	$n = 21$	$n = 17$	2SD	$n = 26$	2SD			27 core	2SD	13 rim	2SD	9 core	2SD	18 rim	2SD		15 core	2SD	9 rim	2SD
wt%											wt%									wt%				
SiO_2	34.37	0.50	34.59	5.46	35.11	34.40	0.70	34.44	0.70	SiO_2		36.63	0.39	36.51	0.34	36.59	0.42	36.64	0.89	SiO_2	47.07	0.61	46.99	0.67
Al_2O_3	18.84	0.64	19.90	7.53	18.55	16.89	0.61	16.94	0.36	Al_2O_3		20.71	0.24	20.67	0.22	20.65	0.20	20.79	0.63	Al_2O_3	31.79	0.34	31.92	0.34
FeO	21.87	1.85	21.58	9.82	21.92	25.50	2.06	24.91	1.22	FeO		35.53	1.22	35.35	0.86	35.76	0.77	35.64	1.17	FeO	13.63	0.36	13.61	0.45
MnO	0.18	0.09	0.18	0.13	0.18	0.27	0.04	0.29	0.06	MnO		4.72	0.71	4.65	0.61	5.24	0.81	5.08	1.34	MnO	0.39	0.09	0.39	0.09
MgO	5.92	0.88	5.72	2.49	5.88	5.15	0.33	4.81	0.29	MgO		1.87	0.39	1.74	0.31	1.60	0.32	1.72	0.46	MgO	4.54	0.16	4.53	0.15
CaO	0.01	0.03	0.02	0.03	0.02	0.02	0.03	0.01	0.03	CaO		0.55	0.10	0.57	0.10	0.58	0.17	0.56	0.16	CaO	0.01	0.02	0.08	0.33
Na_2O	0.15	0.06	0.15	0.26	0.14	0.06	0.13	0.10	0.11	0.04	Total	99.99	1.17	99.49	0.96	100.42	0.85	100.44	1.52	Na_2O	0.20	0.05	0.21	0.04
K_2O	9.75	0.16	9.48	0.48	9.75	9.73	0.18	9.76	0.19											K_2O	0.01	0.02	0.01	0.02
ZnO	0.11	0.05	0.09	0.08	0.06	0.05	0.07	0.09	0.07											Total	97.64	0.84	97.74	0.65
TiO_2	3.54	1.19	2.41	2.82	3.21	0.99	0.26	2.23	0.53															
F	1.07	0.15	0.93	0.37	2.48	0.42	0.17	1.93	0.21															
Cl	0.05	0.02	0.11	0.16	0.11	0.03	0.10	0.50	0.04	*End-members calculated following Deer et al. (1992)*														
Total	95.86	0.70	95.14	1.32	97.39	0.58	1.82	96.02	1.18	Pyrope		7.50	1.57	7.08	1.34	6.44	1.12	6.88	1.72					
F	0.53	0.07	0.46	0.19	1.22	0.20	0.17	1.96	0.21	Almandine		80.13	2.26	80.54	1.30	80.08	1.47	79.97	1.77					
Cl	0.01	0.01	0.03	0.04	0.03	0.01	0.05	0.27	0.03	Spessartine		10.78	1.69	10.72	1.38	11.81	1.89	11.55	3.18					
^{IV}Al	2.63	0.06	2.59	0.36	2.54	0.06	2.52	2.46	0.07	Grossular		1.58	0.26	1.66	0.17	1.64	0.40	1.60	0.40					
$[Fe^{2+}/(Fe^{2+}+Mg)]$	0.67	0.05	0.67	0.10	0.68	0.07	0.02	0.74	0.02	Andradite		0	0	0	0	0	0	0	0	$[Mg/(Mg+Fe_t)]$	37.23	1.29	37.24	1.32

[a] 2SD = 2 Standard deviation.

with sillimanite, apatite, monazite, zircon, ilmenite and rutile as accessory minerals. Garnet, cordierite and perthitic K-feldspar form crystals up to 3 cm, enclosed in a medium-grained (1–5 mm) equigranular matrix (Fig. 4F). Rare biotite occurs as a retrograde mineral, forming rims and other replacement textures around and within garnet. The scarce paleosome, well preserved in tabular schöllen rafts composed of foliated sillimanite-garnet-biotite metagranite, shows the same mineral composition and fabrics of the R14A paleosome (Fig. 4C). It also displays gradual and diffuse contacts with the neosome, suggesting autochthonous partial melting largely controlled by the consumption of biotite. The studied sample M26 only contains neosome, as it was cleaned from all evident paleosome traces.

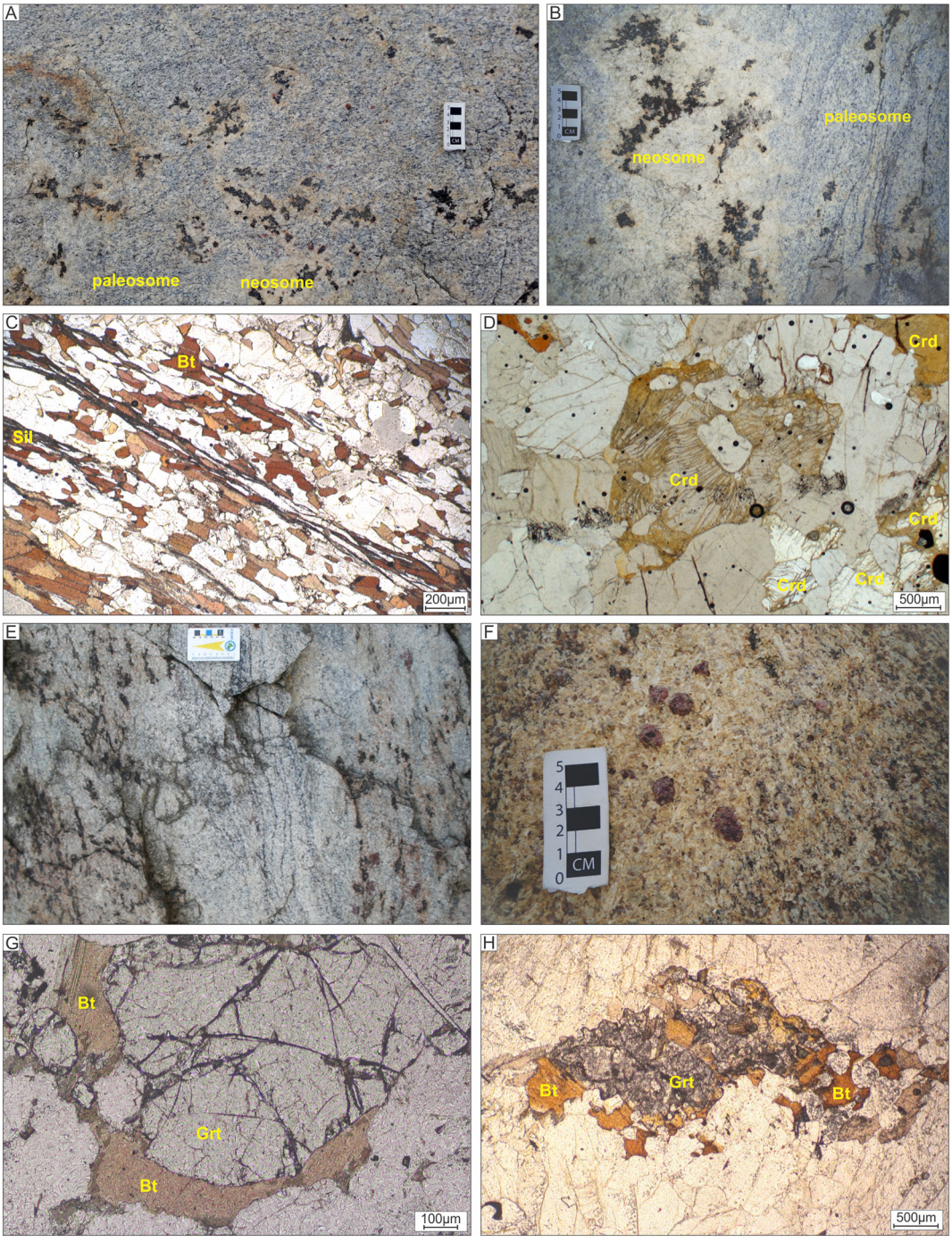

Fig. 4. Host rocks of the Medina batholith: (A) Patch metatexite (R14) composed by paleosome of weakly foliated G2 metagranite (sample R14A), and non-foliated G3 garnet-cordierite neosome (sample R14B); (B) detail of a metatexite composed by paleosome of G2 metagranite, and non-foliated G3 garnet-cordierite neosome; (C) photomicrography (parallel polarizers) of a G2 sillimanite-garnet-biotite metagranite showing well-developed regional foliation outlined by the orientation of biotite (Bt) flakes, stretched quartz and feldspars, and sillimanite (Sil) microneedles (fibrolite); (D) photomicrography (parallel polarizers) of non-foliated G3 neosome, showing weakly to wholly pinitized cordierite (Crd) within the matrix composed of K-feldspar and quartz; (E) nebulitic diatexite rich in G3 garnet-cordierite neosome, and minor paleosome bands of sillimanite-garnet-biotite metagranite and biotite-rich schlieren; (F) detail of G3 garnet-cordierite neosome (sample M26) in nebulitic diatexite with paleosome relicts of foliated sillimanite-garnet-biotite metagranite; (F) photomicrography of M26 neosome, showing rims of late retrograde biotite (Bt) around garnet; (H) photomicrography of M26 neosome, showing late retrograde biotite (Bt) replacing garnet.

3.4. Mineral chemistry of host rocks

The results of complete electron microprobe analyses of K-feldspar, plagioclase, biotite, garnet and cordierite are listed in Tables 2 to 4.

3.4.1. Paleosome - sample R14A

The analyzed K-feldspar, plagioclase, biotite and garnet from paleosome R14A are considered to be metamorphic because they form the regional foliation imprinted in the sillimanite-garnet-biotite metagranite (Fig. 4C). Typical K-feldspar compositions in paleosome R14A range from Or_{81} to Or_{91}; those of plagioclase from An_{14} to An_{17}.

The biotite of the paleosome R14A has siderophyllite-annite contents with $Fe^{2+}/(Fe^{2+}+Mg)$ ranging from 0.63 to 0.71, Al^{IV} from 2.56 to 2.67 a.p.f.u. and TiO_2 from 2.28 to 3.99 wt%.

Garnet forms small crystals to porphyroblasts, both some what stretched along the regional foliation of the paleosome. They are non-zoned grains and present a solid solution of almandine and spessartine reaching >90% of the total composition (Table 4).

3.4.2. Neosomes - samples R14B and M26

Representative K-feldspar compositions range from Or_{84} to Or_{89} in neosome R14B, and varies from Or_{70} to Or_{91} in M26; those of plagioclase from An_{13} to An_{17} and from An_{12} to An_{16}, respectively (Tables 2 and 3).

Garnet is much more abundant in neosome M26 than in sample R14B. Individual crystals do not display any significant major element zonation, with a solid solution of almandine and spessartine reaching >90% of the total composition for both R14B and M26 samples (Table 4). It seems to be a peritectic neoformed mineral.

Large crystals of cordierite occurs in both R14B and M26 neosomes. Cordierite composition corresponds to Fe-rich cordierite with an $Mg/(Mg + Fe^{total})$ ratio of 0.36 to 0.39 (Table 4). It does not occur in the paleosome, being a peritectic mineral crystallized after dehydration melting of biotite.

Textural evidence indicates biotite formation by back reaction in neosome thin sections, which show biotite rim growth over garnet and replacement relations of biotite around and within garnet (Fig. 4G and H). Such features have usually been interpreted as a rehydration process on garnet, during cooling of granitic melts (Fitzsimons, 1996).

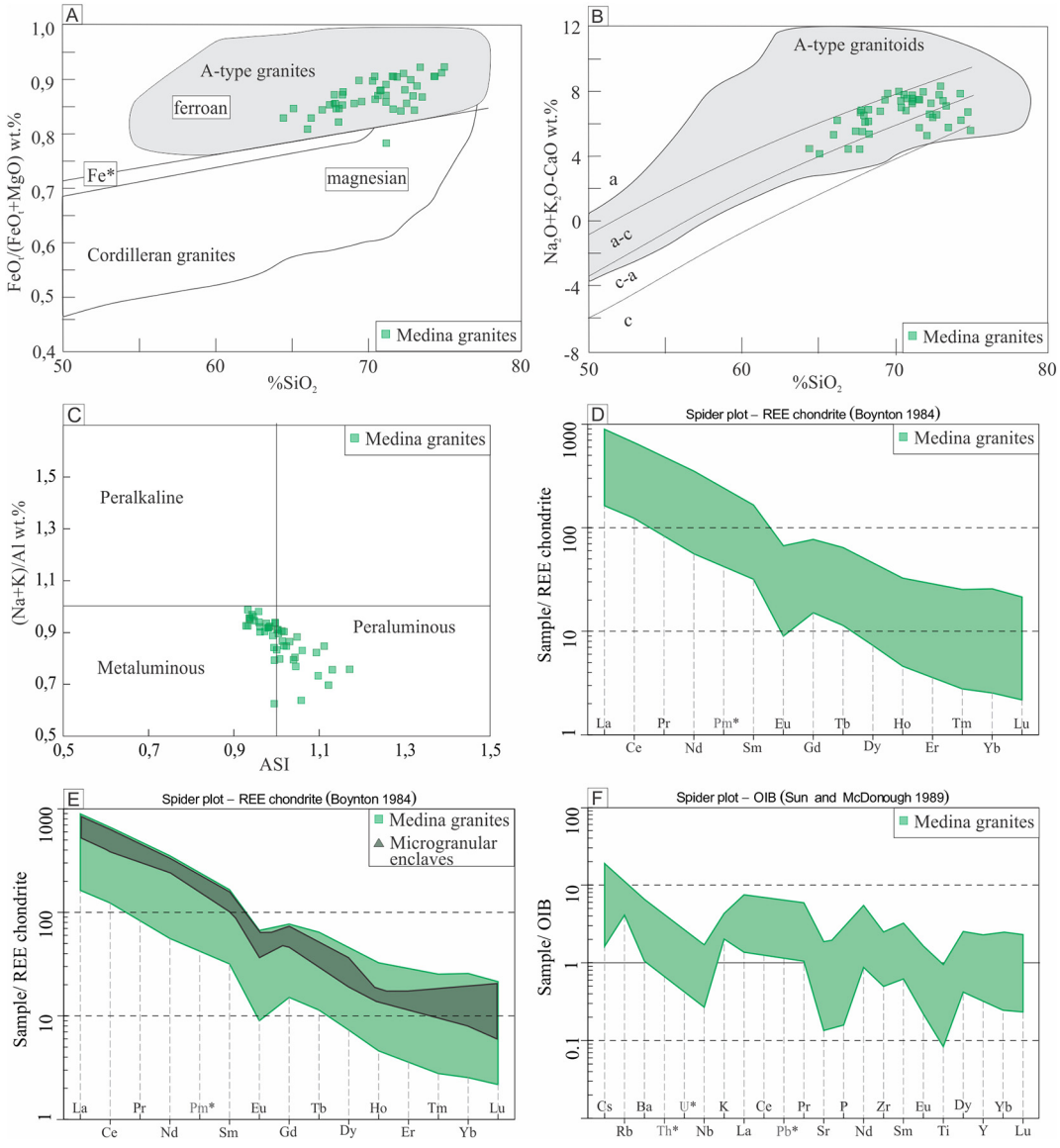

Fig. 5. Lithochemical data from Medina granites plotted on classification diagrams (cf. Frost et al., 2001): (A) $FeO_t/(FeO_t + MgO)$ vs. SiO2 (wt%); (B) $Na_2O + K_2O$ – CaO vs. SiO_2 (wt%); (C) Alumina saturation index (ASI) diagram; (D) Chondrite-normalized REE patterns (normalizing values from Boynton, 1984); (E) Chondrite-normalized REE patterns comparing microgranular enclaves and host granites (normalizing values from Boynton, 1984); (F) multi-elemental spider diagram related to Ocean Island Basalt pattern (OIB, normalizing values from Sun and McDonough, 1989). Data for granites: this work and Paes et al. (2010). Data for microgranular enclaves: this work and Fernandes (1991).

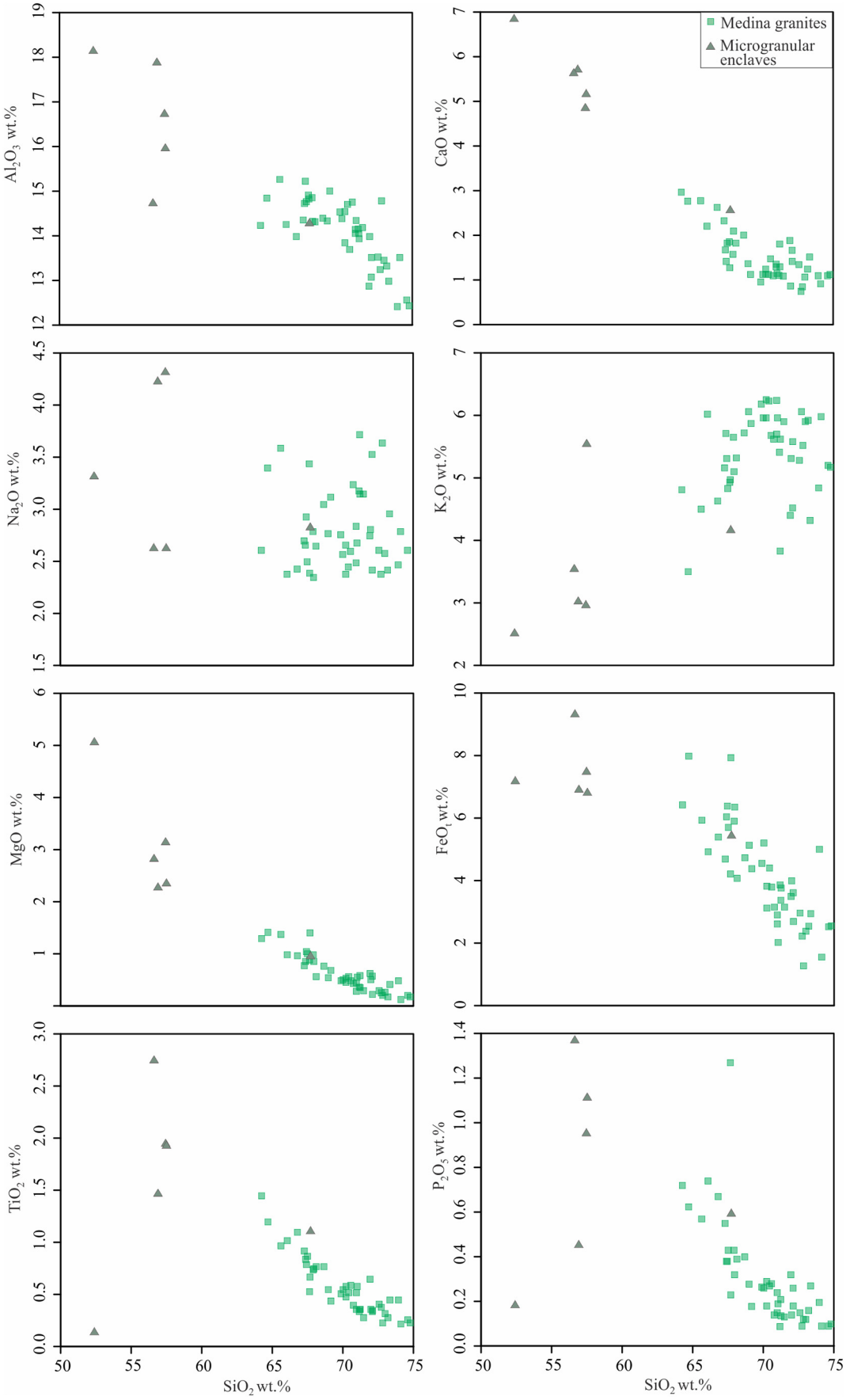

Fig. 6. Lithochemical data from microgranular enclaves and Medina granites plotted in Harker diagrams (data from this work, Paes et al., 2010 and Fernandes, 1991).

Analyzed biotites have siderophyllite-annite contents with $Fe^{2+}/(Fe^{2+}+Mg)$ ranging from 0.46 to 0.70 in R14B, and varies from 0.64 to 0.73 in M26. The content of Al^{IV} range from 1.83 to 2.66 a.p.f.u. in R14B, and from 2.49 to 2.60 a.p.f.u. in M26. The content of TiO_2 is high in both samples (0.06–3.95 wt% in R14B; 2.07–4.00 wt% in M26), being negatively correlated with Al_2O_3 (Table 4).

4. Whole-rock geochemistry

Together with mineral assemblages, lithochemical studies are useful to detail the classification and support petrogenetic interpretations on the studied rocks.

4.1. Medina granites – major and trace elements

The Medina granites are clearly A-type ferroan granites with FeOt/(FeOt+MgO) ratios above 0.77 for $SiO_2 > 65$ wt% (Fig. 5A), calc-alkalic to alkali-calcic (Fig. 5B), and weakly peraluminous to metaluminous reaching the border of the peralkaline field (Fig. 5C).

The REE patterns for Medina granites, represented in a chondrite-normalized diagram, show enrichment of LREE ([La/Yb] N average = 48 to 59), and negative Eu anomalies ((Eu / Eu *) N 0.45) (Fig. 5D), as usual in A-type granites (Nardi and Bitencourt, 2009). The microgranular enclaves show a quite similar pattern (Fig. 5E), being enriched in LREE ([La/Yb] N average = 52 to 68), with negative Eu anomalies ((Eu / Eu *) N 0.61). SiO_2 contents range from 64 to 75 wt% in Medina granites, whereas the microgranular enclaves show lower values (from 52 to 67 wt%). From a geochemical viewpoint (Fig. 6), these rocks commonly display two different trends in Harker diagrams. One of them, including FeOt, MgO, TiO_2 and CaO, is characterized by negative correlation with increasing evolution, whereas K_2O trend shows positive correlation. The linear variations in Harker diagrams together with similar REE signatures suggest genetic links between microgranular enclaves and their host Medina granites.

Data from granites normalized to OIB (Sun and McDonough, 1989) display a relatively flat general pattern (Fig. 5F) with enrichment of most incompatible elements, as expected since the rocks are more differentiated than the OIB standard. Negative anomalies are noticed for Ba, Nb, Sr, P and Ti. Normalization using the OIB patterns suggests geochemical similarity with magmas derived from such sources. The Medina granites have medium to high contents of high field-strength elements (HFSE) such as Zr (139–663 ppm), Y (9–59 ppm), Nb (13–59 ppm) and Ce (100–500 ppm). Total Zr + Nb + Ce + Y average contents are 765 ppm (our samples) and 722 ppm (samples from Paes et al., 2010), as expected for A-type granites (>350 ppm, Whalen et al., 1987). These features suggest chemical similarity of the Medina granites with those originated mainly by fractionation of basic magmas produced from mantle-enriched sources. However, further studies with more powerful analysis (e.g., isotope geochemistry) are needed to an ultimate test on that hypothesis.

Diagrams for tectonic environment discrimination indicate that the Medina granites were formed in within-plate continental setting (Fig. 7A), with some deviations to other fields probably due to host rock contamination and/or crustal inheritance from magma sources. In A-type granite discriminant diagrams (Whalen et al., 1987), the Medina granites behave as typical A-type granites (Fig. 7B, C, and D). Only the samples that plot in the within-plate granite field and are A-type rocks in Whalen et al. (1987) diagrams were tested for the A1-A2 discrimination diagram of Eby (1992). Accordingly, most Medina granites plot in the A1 field (Fig. 7E and F), suggesting they may have a genetic similarity with differentiates of magmas derived from sources like those of oceanic-island basalts, but emplaced in continental rifts or during intra-plate magmatism related to mantle plumes or hotspots (*cf.* Eby, 1992).

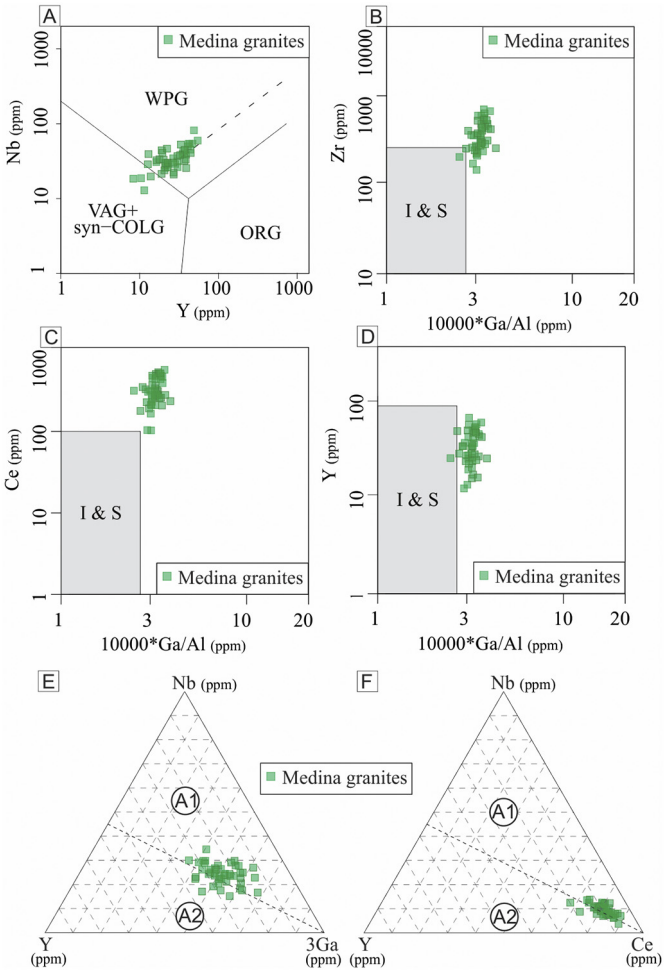

Fig. 7. Lithochemical data from Medina granites plotted on discriminant diagrams: (A) Y vs. Nb (Pearce et al., 1984). B to D (Whalen et al., 1987): (B) 10,000 * Ga/Al vs. Zr, (C) 10,000 * Ga/Al vs. Ce, and (D) 10,000 * Ga/Al vs. Y. Triangular diagrams E and F (Eby, 1992): (E) Y-Nb-3Ga; and (F) Y-Nb-Ce. Data for granites: this work and Paes et al. (2010).

4.2. Host rocks – major and trace elements

Lithochemical analysis on host rocks were carried out from paleosome and neosome samples, which were carefully separated and cleaned one from each other. From paleosome to neosome samples, they generally vary from magnesian to ferroan (Fig. 8A), calc-alkalic to alkali-calcic (Fig. 8B), and from striking peraluminous (ASI = 1.3–1.0), to very slightly metaluminous (ASI = 0.95–1.0) (Fig. 8C).

Paleosome and neosome samples have moderate to high abundance of rare-earth elements (REE = 86–417 ppm and 44–445 ppm, respectively), with significant negative Eu anomalies (Eu/Eu * = 0.65 for paleosome and 0.50 for neosomes, and pronounced enrichment of LREE ([La / Yb] N average = 34 and 39, respectively; Fig. 8D).

Primitive-mantle normalized spider diagrams also display similar patterns for both sample sets, showing marked negative anomalies for Ba, Sr and Ti, significant enrichment in Rb, and low contents of high field strength elements (HFSE) such as Zr (130 ppm), Nb (19 ppm) and Y (16 ppm) (Fig. 8E).

5. Zircon and monazite U—Pb geochronology

U—Pb zircon and monazite ages obtained in our study are presented in Figs. 9 to 10. These analysis were performed on samples: i) R13A, Medina A-type granite (Fig. 9A,B and 10A); ii) R14A, paleosome of a

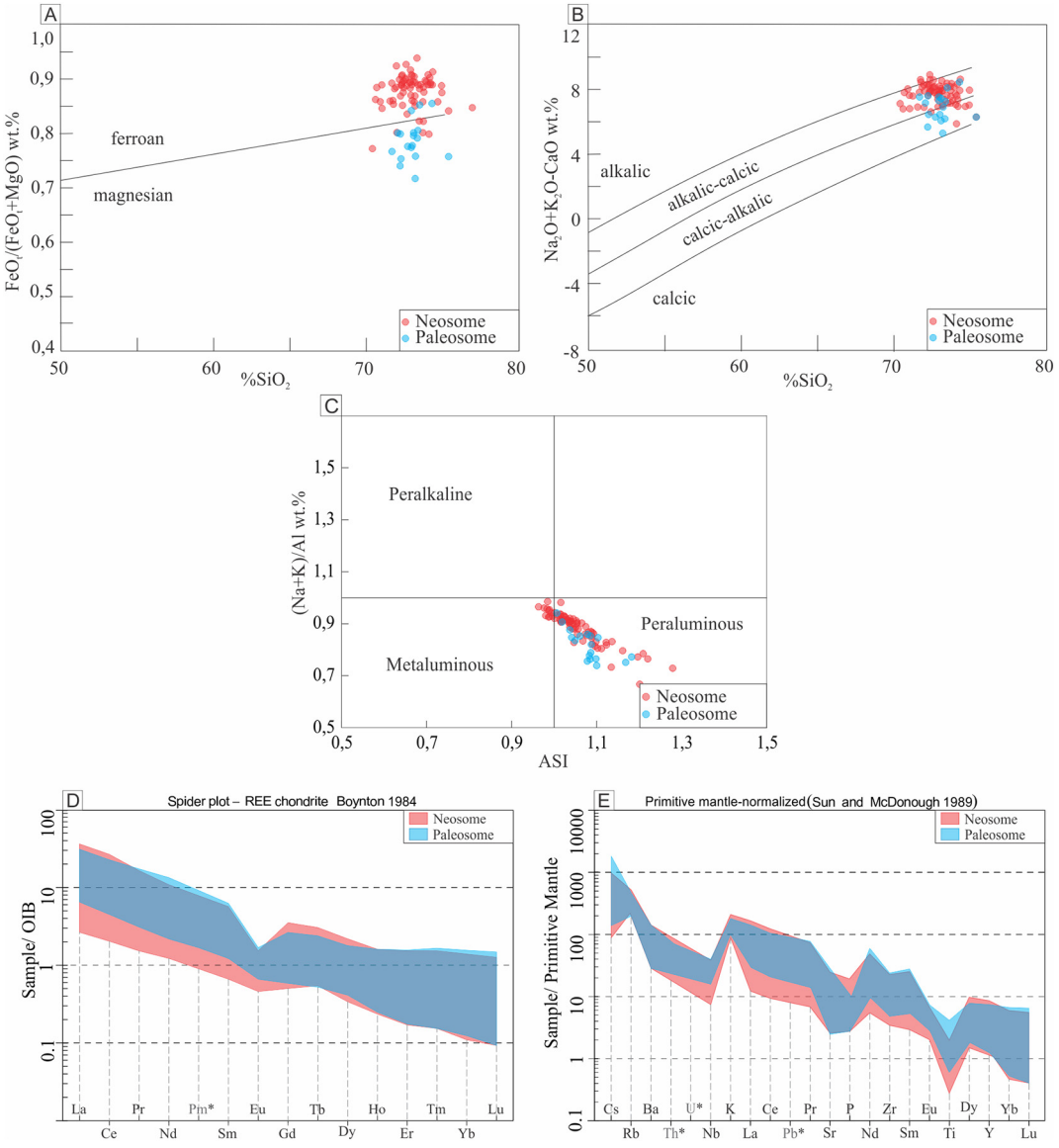

Fig. 8. Studied host rocks plotted on classification diagrams (cf. Frost et al., 2001): (A) FeOt/(FeOt + MgO) vs. SiO2 (wt%); (B) Na2O + K2O – CaO vs. SiO2 (wt%); (C) Alumina saturation index (ASI); (D) Chondrite-normalized REE patterns (normalizing values from Boynton, 1984); (E) Primitive mantle-normalized spider diagram (normalizing values from Sun and McDonough, 1989). Data for host rocks: this work and Paes et al. (2010).

metatexite (Fig. 9C–F and 10B); iii) R14B, neosome of the same metatexite (Figs. 10C and 11) and, iv) M26, neosome of a diatexite close to the contact with the Medina granite represented by sample R13A (Figs. 10 and 12).

5.1. Sample R13A – Medina granite

Zircon crystals from a typical Medina granite (R13A) range from 150 to 320 μm in size with length to width ratios of 2:1 and 3:1 to 4:1. Some grains are needle-shaped (acicular) zircon crystals suggesting quick crystallization. Zircon zoning is poorly developed and commonly shows dark core surrounded by a bright luminescent area followed by low luminescent border (Fig. 9A). The compositional difference in intermediate growth zoning becomes very small, yielding only faint zoning patterns in most of the grains. If the zoning pattern can be noticed, it is observed that regular growth zoning is interrupted by textural discontinuities along which the original zoning is resorbed and succeeded by the deposition of new-growth-zoned zircon. In some grains, it is possible to identify bright seams that indicate altered fractures disrupting original zoning. Twenty-one spot analyses on zircon crystals reveal relatively low Th/U values (0.12–0.33) and yield a Concordia age of 501 ± 2 Ma (MSWD = 1.7, Fig. 9B).

Monazite grains from the R13A Medina granite are anhedral, generally 85–200 μm in size with most being around 135 μm. BSE imaging indicates the presence of weakly zoned grains whereas other are non-zoned. Twenty-eight spot analyses on monazite grains, with Th/U ratios from 12 to 33, furnished a mean $^{207}Pb/^{235}U$ age of 497 ± 2 Ma (95% conf., MSWD = 1.9; Fig. 10A).

5.2. Host rock samples

U—Pb (LA-ICP-MS) analysis were performed on zircon and monazite grains extracted from a paleosome (R14A) and related neosome (R14B) of a metatexite located relatively far from the Medina batholith, and from the neosome of the diatexite located very close to the contact with the Medina granite.

5.2.1. Paleosome from metatexite - sample R14A

In paleosome R14A, zircon crystals range from 75 to 225 μm in size with elongation ratios varying from 2:1 to 7:1; the most common are

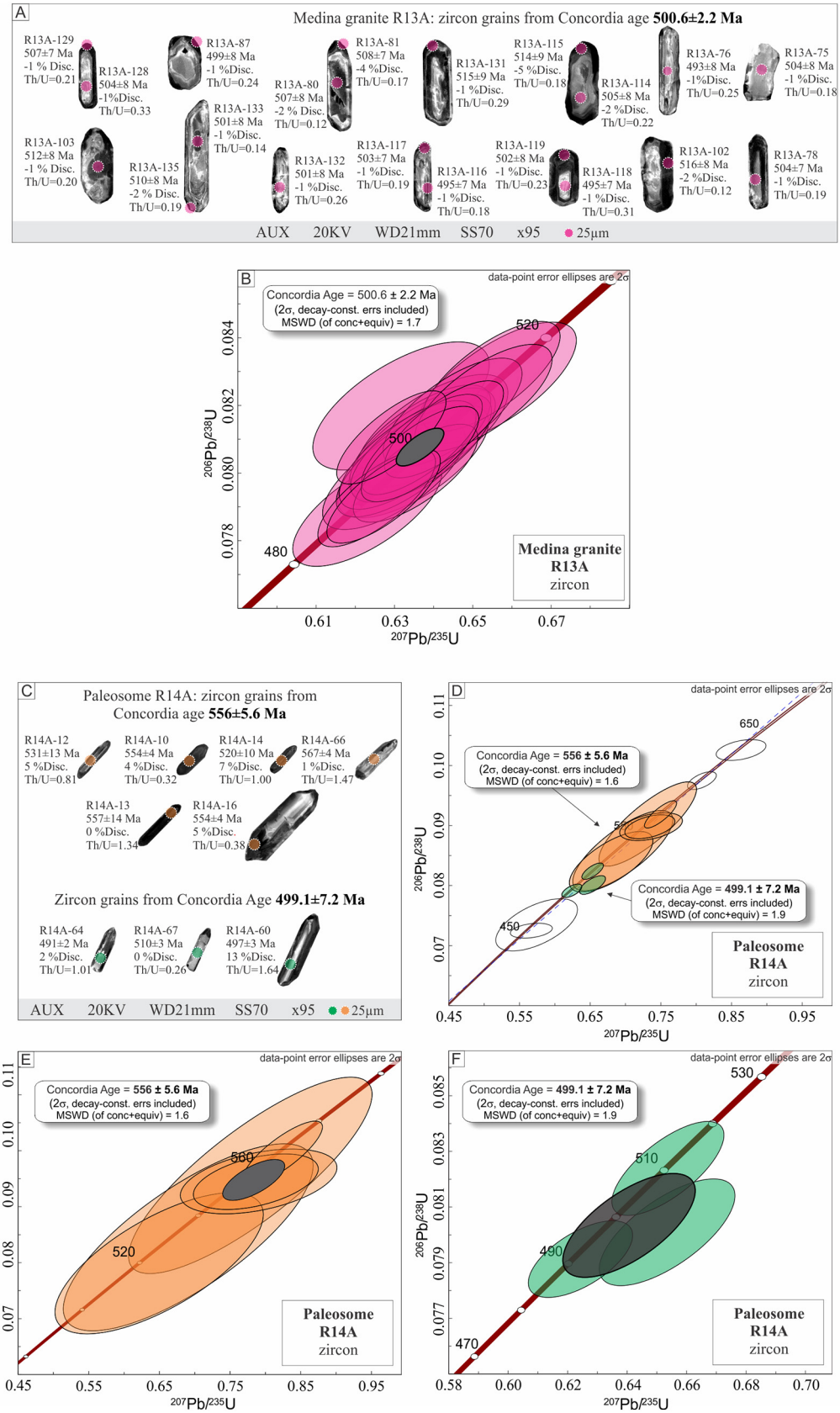

Fig. 9. Cathodoluminescence images on analyzed zircon grains and U—Pb Concordia diagrams for: (A) and (B), Medina granite R13A; (C), (D), (E) and (F) paleosome R14A.

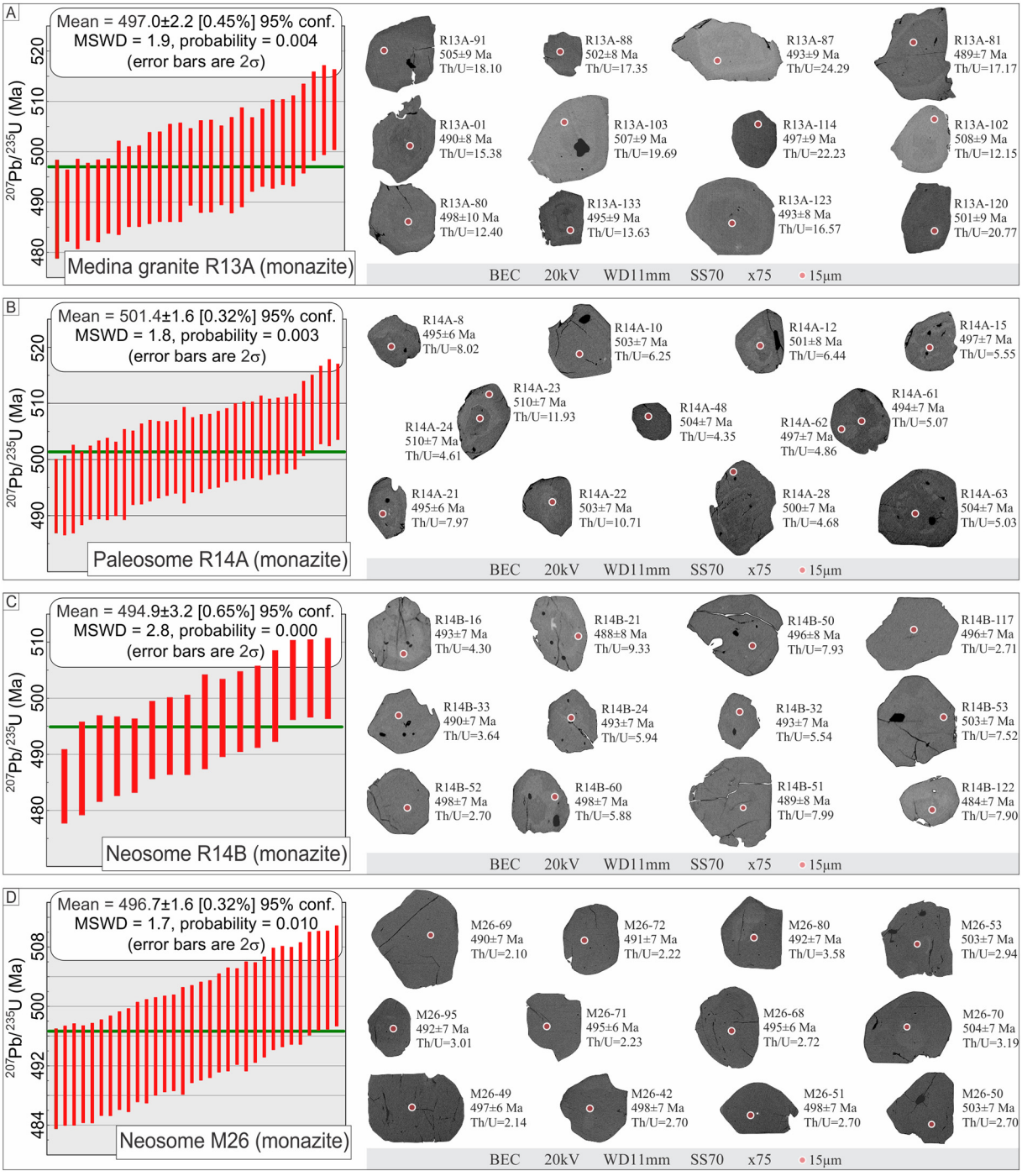

Fig. 10. U—Pb data and electron backscatter diffraction images for monazite crystals from: (A) Medina granite R13A. Host rocks: (B) paleosome R14A; (C) neosome R14B; and (D) neosome M26.

3:1, 4:1 and 5:1. Combined SEM-CL and optical images reveal mostly elongate prismatic crystals with discrete oscillatory zoning, and subhedral to euhedral rims (Fig. 11A, B).

Although significant spreading along the Concordia from ca. 630 Ma to ca. 450 Ma, thirteen spot analysis may yield two Concordant ages (Fig. 11C, D, E). Six spots with Th/U = 0.32–1.47 and CL image features of igneous grains generated a Concordia age of 556 ± 6 Ma (MSWD = 1.6, Fig. 11D), which may be related to the magmatic crystallization of the paleosome igneous protolith. Three spots (Th/U = 0.26–1.64) yield a Concordia age of 499 ± 3 Ma (MSWD = 1.5, Fig. 11E), which is virtually equal to the zircon magmatic age of 501 ± 2 Ma given by the Medina granite (R13A sample; Fig. 9).

Monazite grains from the paleosome R14A are anhedral and rounded, ranging from 75 to 200 µm in length (Fig. 10B). BSE image indicates the presence of weakly zoned grains, whereas others seem to be non-zoned. There is no age variation associated with the observed zoning. Fifty two spot analyses in R14A monazite, with Th/U ratios of 4–20, yield a mean $^{207}Pb/^{235}U$ age of 501 ± 2 Ma (95% conf., MSWD = 1.8; Fig. 10B).

5.2.2. Neosome from metatexite – sample R14B

This sample contains 125 to 250 µm, prismatic, subhedral to euhedral or sub-rounded-shaped zircon grains with elongation ratios varying from 2:1 to 4:1. CL image displays concentric and convolute

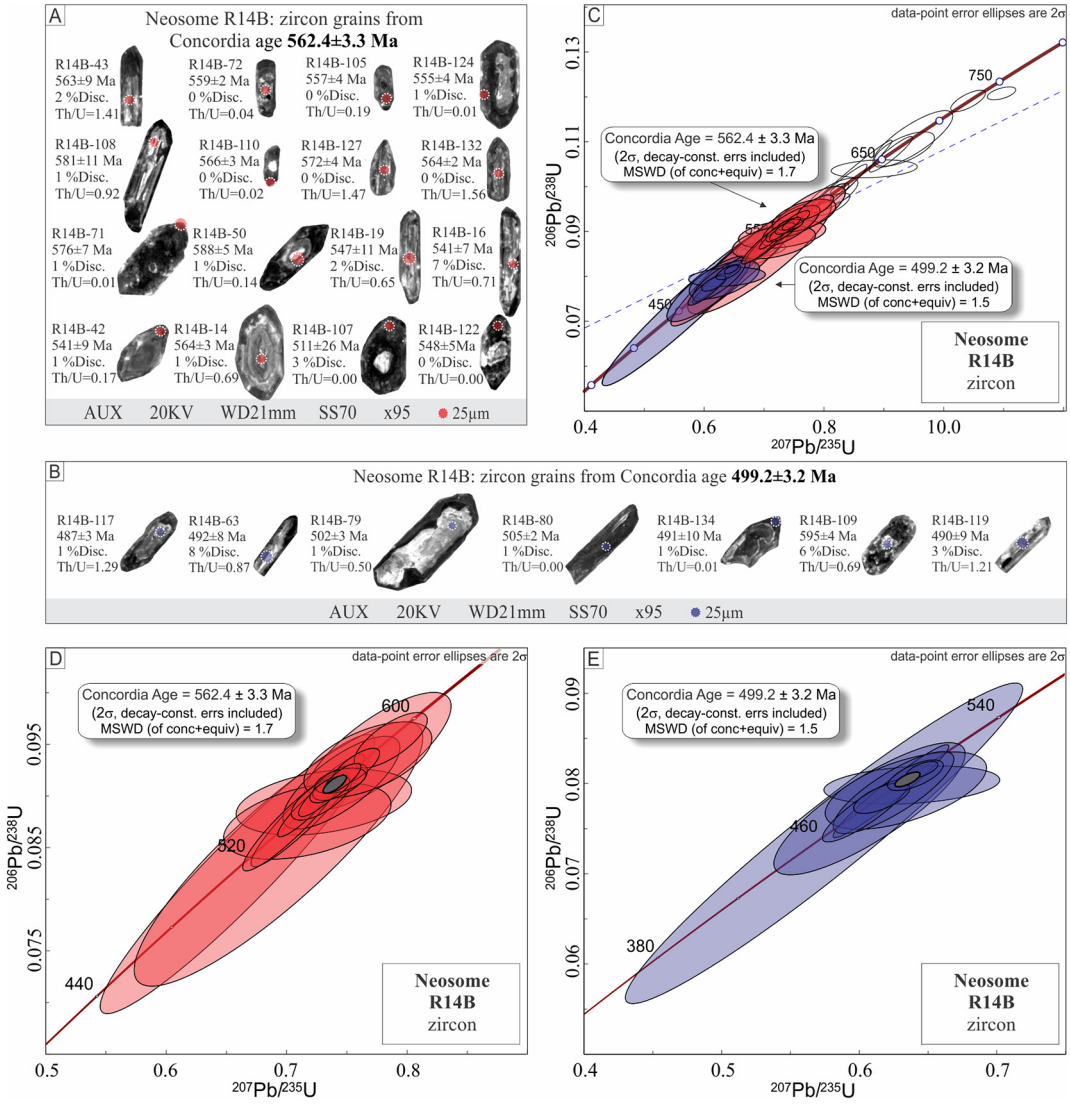

Fig. 11. Cathodoluminescence images from zircon grains and U—Pb Concordia diagrams for neosome R14B.

zoning, typical of high-grade metamorphic zircon (e.g., Vavra et al., 1999). Xenocrystic cores and grain discontinuities indicate deep resorption of early zircon phases (Fig. 11A,B). Some grains show complex growth zoning with local intermediate resorption.

Although spreading along the Concordia from ca. 750 Ma to 450 Ma, data from fifty-four spots generated two Concordia ages (Fig. 11C, D, E). Eighteen spot analyses on zircon have variable Th/U ratios (0.00–1.60) and yield a Concordia age of 562 ± 3 Ma (MSWD = 1.7, Fig. 11D), which is similar to the age of the R14A paleosome protolith (556 ± 6 Ma), although some Th/U ratios suggest a metamorphic event. Ten analyses from the younger population (Th/U = 0.00–1.50) produced a Concordia age of 499 ± 3 Ma (MSWD = 1.5, Fig. 11E), very similar to the youngest zircon and monazite ages from the paleosome and, also, the magmatic ages for the Medina granite.

Monazite from sample R14B is up to 200 µm in size but is generally around 100–130 µm (Fig. 10C). Grains are usually rounded, anhedral to subhedral and a few of them also contain cracks and holes. Under BSE imaging, grains are commonly weakly zoned to non-zoned. Sixteen spot analyses in R14B monazite, with Th/U values of 2.7–9.3, generate a mean $^{207}Pb/^{235}U$ age of 495 ± 3 Ma (95% conf., MSWD = 1.8; Fig. 10C).

5.2.3. Neosome from diatexite – sample M26

Zircon grains from neosome M26 are prismatic, subhedral, ranging from 108 to 350 µm in size with elongation ratios varying from 2:1 to 6:1. CL images reveal convoluted zoning and cores truncated by irregular zoning, which is interpreted as being a recrystallization feature typical of granulite facies zircon. Inherited cores and grain discontinuities indicate deep resorption of early zircon phases (Fig. 12A, B).

Spot ages spread along the Concordia from ca. 650 Ma to ca. 480 Ma, but show two clear age clusters (Fig. 12C, D, E). Sixteen spot analyses on zircon have Th/U values of 0.00–1.20 and yield a Concordia age of 564 ± 2 Ma (MSWD = 1.03, Fig. 12D), again in good agreement with the oldest Concordia ages obtained for samples R14A and R14B. Nine analyses (Th/U = 0.00–1.70) from the younger population produced a Concordia age of 507 ± 3 Ma (MSWD = 1.06, Fig. 12E), roughly similar to the youngest ages yielded by zircon clusters of the previously described samples.

Monazite grains are anhedral to sub-rounded (Fig. 10D), <200 µm in diameter, usually around 150 µm, and BSE image shows non-zoned grains, whose sixteen spots have a mean $^{207}Pb/^{235}U$ age of 495 ± 3 Ma (95% conf., MSWD = 1.8; Fig. 10D) and Th/U = 2.7–9.3.

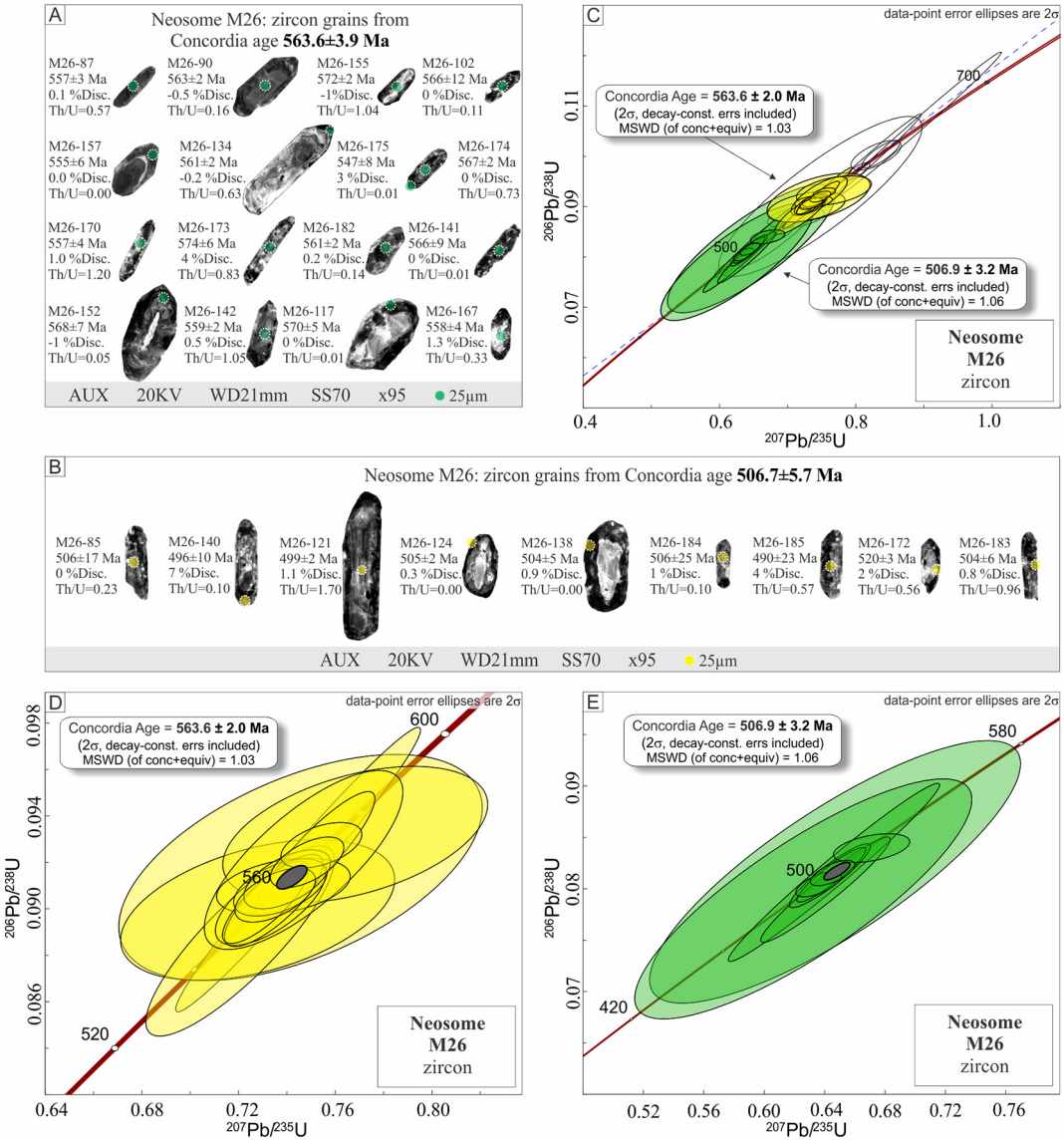

Fig. 12. Cathodoluminescence images from zircon grains and U—Pb Concordia diagrams for neosome M26.

6. P-T conditions

The P-T conditions recorded by the non-foliated garnet-cordierite neosome (M26), separated from a diatexite found close to the contact with the Medina granite (R13A), were investigated by phase equilibrium calculations in the chemical system MnO–Na_2O–CaO–K_2O–FeO–MgO–Al_2O_3–SiO_2–H_2O–TiO_2–Fe_2O_3 (MnNCKFMASHTO), using THERIAK-DOMINO software (De Capitani and Petrakakis, 2010), in combination with the updated td-tcds62-6axmn-03.txt converted Holland and Powell (2011) database. Mineral abbreviations are: Ms. – white mica; Bt – biotite; Grt – garnet; Crd – cordierite; Ky – kyanite; Sil – sillimanite; And – andalusite; Pl – plagioclase; Kfs – K-feldspar; Ilm – ilmenite; Spl – spinel; Rt – rutile; H_2O – pure water; Liq – silicateliquid/melt; Qtz – quartz. Pseudosection was calculated using the bulk composition from the same sample M26.

Appropriate values for water content were investigated on T-X pseudosections and the bulk H_2O values (M26 = 0.03 wt%) were chosen according to the methodology of White et al. (2001).

For the neosome M26, the mineral assemblage Pl-Kfs-Grt-Crd-Ilm-Qz-Sil is stable between 660 and 860 °C at 2.0–3.8 kbar (Fig. 13A). Within this field, the amount of garnet (2–10 vol%) and cordierite (8–25 vol%) is compatible with the modal contents estimates in thin section (~3% and 15%, respectively). The modeling shows a rise in the Crd mode, conjugated with a decrease in the Grt mode if decompression occurs and/or temperature increases over the range defined by the peak assemblage.

Modeled garnet shows compositional isopleths of X_{Alm}, measured mineral composition of Grt yield X_{Alm} values ranging from 0.80 to 0.81 (Fig. 13B). Fig. 13C shows compositional Crd Mg# isopleths, as well as one highlighted zone can be outlined by measured compositions yielding Crd Mg# that range from 37 to 39. The use of X_{Alm} and Crd Mg# values helps to more tightly constrain the P-T conditions of the peak assemblage to 750–840 °C and 2.4–3.5 kbar (Fig. 13D).

7. Discussion

The presented data allow us to discuss the nature and origin of a thermal-magmatic rebound during the post-collisional stage in the ensialic sector of the northern Araçuaí orogen, focusing the Medina batholith and its host rocks.

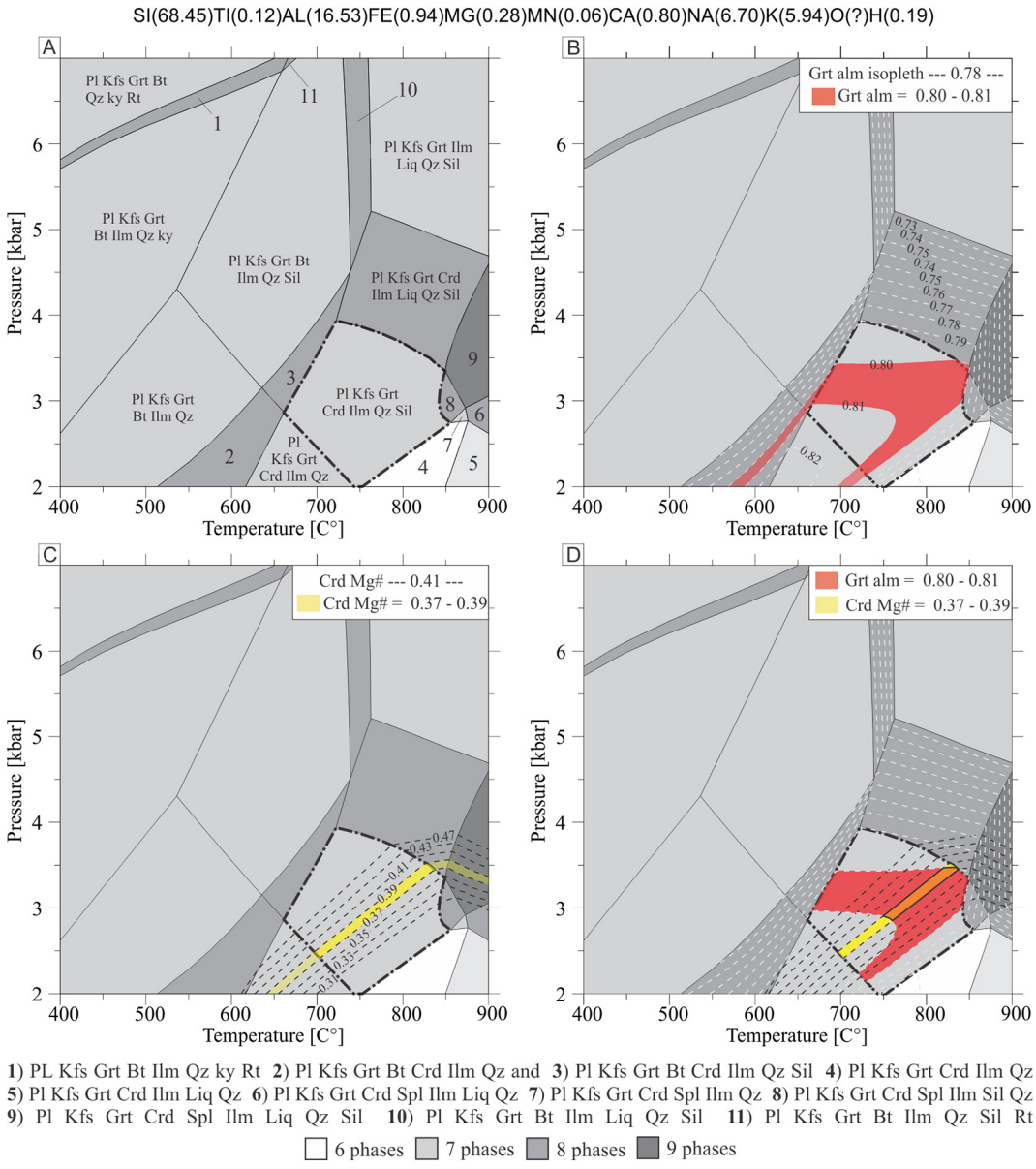

Fig. 13. Calculated P-T pseudosections for neosome M26 on a whole-rock bulk composition that is presented at the top of the diagrams in moles. (A) P-T fields of peak assemblage Pl-Kfs-Grt-Crd-Ilm-Qz-Sil (bold line); (B) Plot of compositional isopleths of X_{Alm}; (C) Plot of compositional Crd Mg# isopleths; (D) P-T conditions of equilibration estimated based on overlapping of all the highlighted zones of composition (B and C).

7.1. Petrogenesis of the Medina batholith

The Medina batholith mostly includes biotite-bearing syenogranite to monzogranite with a ferroan, alcali-calcic to calc-alkalic, metaluminous to weakly peraluminous signature. In general, the Medina granites have HFSE abundances (Zr + Nb + Ce + Y > 700 ppm) and high Ga/Al ratios (Fig. 7B, C, and D), which are features typical of A-type granites (*cf.* Whalen et al., 1987).

The Zr saturation geothermometry (T_{Zr} = 12,900 / [2.95 + 0.85 M + ln(496,000/Zr_{melt})]) may provide good estimates of crystallization temperatures for both metaluminous and peraluminous rocks (Miller et al., 2003; Watson and Harrison, 1983). In order to calculate the Zr saturation temperature, a chemical analysis for major elements must be done, from which the cation ratios are calculated and then the M determined. Once an M value is calculated, one must determine if the sample falls within or outside of the calibration range of the Watson and Harrison (1983) experiments (M = 1.0–1.5). If the calculated M value lies within the experimental range of Watson and Harrison (1983), then the user may feel relatively confident that the calculated M can provide useful Zr saturation and temperature information. This compositional factor M [(Na + K + 2Ca)/(Al x Si)] displays values between 1.2 and 1.5, which is a reliable calibration range for the Zr saturation geothermometry (*cf.* Hanchar and Watson, 2003). Accordingly, this geothermometer indicates a temperature range of 760–930 °C (Fig. 14A), which can be related to the crystallization of Medina granites but also, concerning the highest values, to melting conditions in the magma source. Such high melt temperature is not usually achieved in the crust, requiring the involvement of mafic magmas and/or a high mantle heat flow (*cf.* Eby, 1992; Bonin, 2007).

The Medina granites belong to the oxidized A-type (Fig. 14B,C), which are geochemically distinct from I-type calc-alkaline or Cordilleran granites, but are similar to typical A-type granites in most attributes, including those with rapakivi texture (Dall'Agnol and Oliveira, 2007). Experimental data indicate that, besides pressure, the nature of A-type

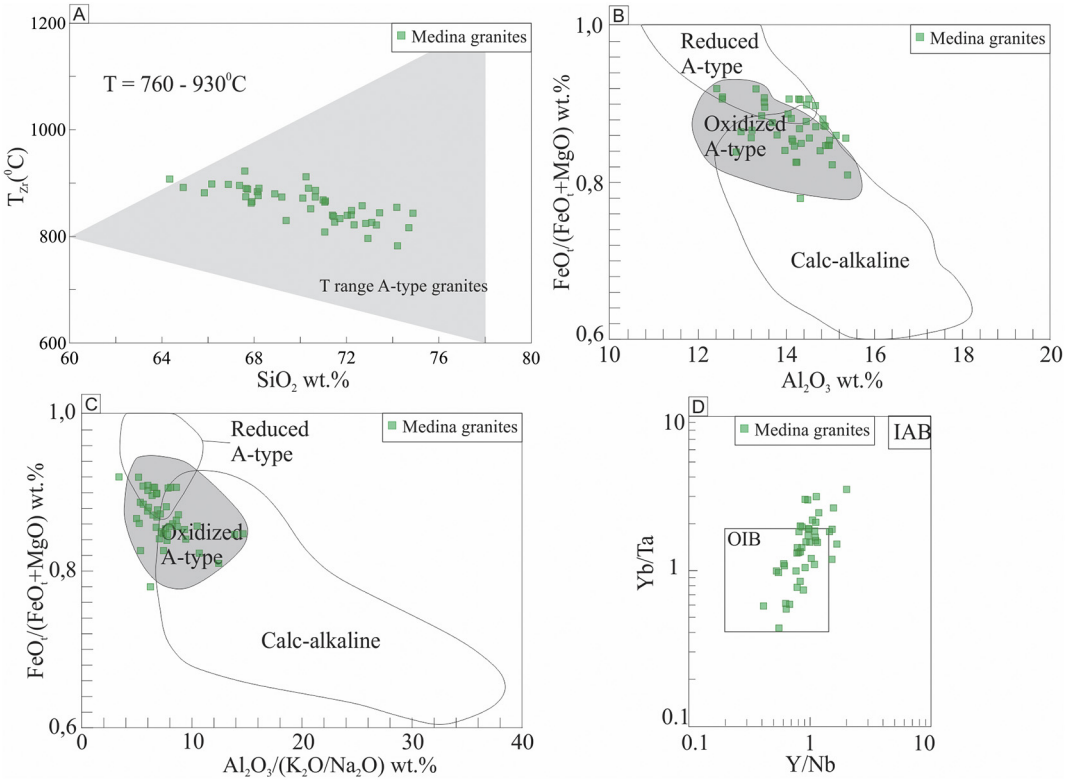

Fig. 14. (A) Zr saturation temperatures TZr (°C) were calculated following Miller et al. (2003) and Dahlquist et al. (2010). Geothermometer was calibrated for M = 1.2 to 1.5, and indicates a temperature range of 760 - 930 °C for the Medina granites. (B) Whole-rock FeOt/(FeOt+MgO) vs. Al2O3, and (C) FeOt/(FeOt+MgO) vs. Al2O3/(K2O/Na2O) (cf. Dall'Agnol and Oliveira, 2007). (D) Y/Nb versus Yb/Ta plots for Medina granites. Fields for Oceanic Island Basalts (OIB) and Island Arc Basalts (IAB) are from Eby (1990). Data for granites: this work and Paes et al. (2010).

granites is dependent on both fO_2 conditions and water contents of magma sources. Oxidized A-type magmas are considered to be derived from melts with substantial H_2O contents, originating from partial melting of quartz-feldspathic igneous sources under oxidizing conditions in the lower crust (Dall'Agnol and Oliveira, 2007; Dall'Agnol et al., 1999).

Both enclaves and host Medina granites show LREE-enriched, significant negative Eu anomalies and flattening HREE end-segment (Fig. 5E). These REE patterns and close chemical coherence in Harker diagrams (Fig. 6) suggest a genetic link between enclaves and host granites, probably involving fractional crystallization of the major igneous phases from a series of comparable (cogenetic) magmatic phases. Except for K_2O, all major element oxides gradually decrease with increasing SiO_2 content. Particularly, increases in SiO_2, K_2O and decreases in FeOt, MgO, TiO_2 and CaO contents are consistent with their evolution through fractional crystallization processes (i.e., plagioclase fractionation).

The studied A-type granites display a chemical similarity to OIB (Fig. 14D), suggesting relation to an OIB-like source. Variations can be explained by the high degree of fractionation of feldspar (negative Ba, Sr and Eu anomalies), apatite (negative P anomaly) and opaque oxide minerals (negative Ti anomaly). Feldspar fractionation plays an important role in the evolution of A-type granites worldwide (Dall'Agnol et al., 2005; Deng et al., 2016; Eby, 1990; King et al., 2001; Vallinayagam and Kochhar, 2011; Whalen et al., 1987).

In summary, the Medina granites notably represent within-plate A1-type felsic magmas geochemically similar to those related to sources with oceanic-island basalt (OIB) signature (Fig. 14D). Such A1-type granites are mostly found in extensional tectonic settings (e.g., active continental rifts and post-collisional or post-orogenic extensional settings) driven by mantle plumes or hotspots.

7.2. Zircon and monazite dating evidence

Independently if the sample came from a metatexite or diatexite, the studied paleosome and neosome samples furnished two zircon U—Pb age clusters: the oldest at around 560 Ma (556 ± 11 Ma for paleosome R14A; 558 ± 5 Ma for neosome R14B; and 563 ± 4 Ma for neosome M26), and the youngest at around 500 Ma (499 ± 7 Ma for paleosome R14A; 499 ± 3 Ma for neosome R14B; and 507 ± 3 Ma for neosome M26). Otherwise, all U—Pb monazite ages only cluster around 500 Ma (501 ± 2 Ma for paleosome R14A; 495 ± 3 Ma for neosome R14B; and 497 ± 2 Ma for neosome M26). Both the youngest zircon and monazite ages are identical, within analytical error, to both U—Pb zircon (501 ± 2 Ma) and monazite (497 ± 2 Ma) ages for the typical Medina granite (sample R13A).

The oldest age (ca. 560 Ma), obtained from oscillatory-zoned zircon crystals with typical igneous Th/U ratios, much probably represents the magmatic crystallization of the paleosome granitic protolith (Fig. 9E). Actually, this interpretation is in very good agreement with the regional age range for most metagranites of the collisional G2 supersuite (*cf.* Melo et al., 2017a,b; Gradim et al., 2014; Pedrosa-Soares et al., 2011; Richter et al., 2016; Table 1). Similar Concordia ages around 553–563 Ma, furnished by the garnet-cordierite neosomes (samples R14B and M26), indicate zircon inheritance from the G2 paleosome (Figs. 11D, 12D). Indeed, the studied neosomes show gradual and diffuse contacts with their related paleosomes, and contain biotite-rich schlieren resembling relicts of the paleosome foliation. This zircon inheritance, together with fabrics relations and geochemical trends, strongly suggest that the garnet-cordierite neosome formed from autochthonous partial melting of the foliated sillimanite-garnet-biotite metagranite (G2 paleosome).

In fact, the youngest zircon ages recorded in the studied paleosome and neosome samples are virtually equal to the magmatic

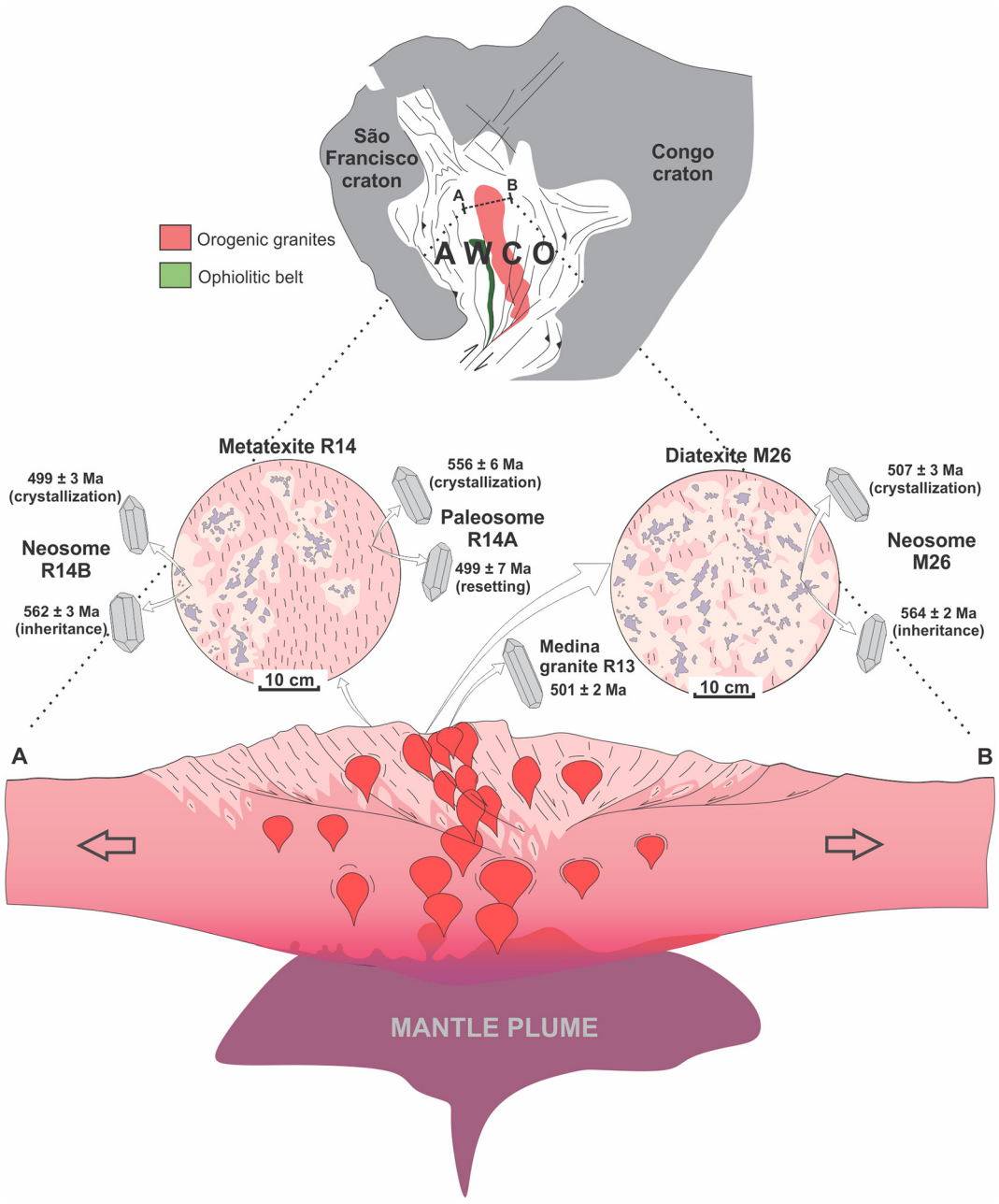

Fig. 15. Model illustrating a rising mantle plume during the gravitational collapse of the northern sector of the Araçuaí – West Congo orogen (AWCO), related to the generation of the Medina granites and post-collisional anatexis on country rocks.

crystallization age of the Medina granite (Fig. 9B), all of them around 500 Ma (Figs. 9F, 11E, 12E), implying that those minerals also formed and/or recrystallized concurrently in a late orogenic stage at high temperature. Together, those youngest U—Pb ages suggest that an abnormally hot source imposed an important thermal process on the host rocks, causing isotopic resetting and partial melting. Indeed, a clear evidence for such a vigorous thermal process is the emplacement of the Medina batholith itself, suggesting high temperature metamorphism and anatexis within contact metamorphism aureoles. However, evidence of a Late Cambrian thermal event has been reported from several regions of the Araçuaí orogen, either for areas with exposed post-collisional G4 and/or G5 intrusions (De Campos et al., 2004, 2016; Gradim et al., 2014; Melo et al., 2017a,b; Pedrosa-Soares et al., 2011; Pedrosa-Soares and Wiedemann-Leonardos, 2000; Peixoto et al., 2018; Richter et al., 2016) or far from them (Cabral et al., 2017; Marshak et al., 2006; Queiroga et al., 2016). It has also been suggested that some garnet-cordierite neosomes ascribed to the G3 supersuite could be related to the same thermal event that formed G5 intrusions (Pedrosa-Soares et al., 2011).

7.3. Thermobarometric modeling: evaluating the magnitude of a thermal influx

The P-T conditions of 750–840 °C at 2.4–3.5 kbar, constrained by the peak assemblage (Pl-Kfs-Grt-Crd-Ilm-Qz-Sil; Fig. 13) are consistent with a process of incongruent melting reactions consuming biotite and sillimanite under water-undersaturated and high-T conditions. The absence of amphiboles and low modal proportion of cordierite in the studied neosomes could be used to reinforce the minimum H_2O content of the parental magma. The breakdown of biotite has a solid knowledge basis either from experiments and detailed studies involving themobarometric modeling on high-grade peraluminous migmatites

(Johnson et al., 2008; Nicoli et al., 2015; Patiño Douce and Beard, 1996; Stevens et al., 1997; Vielzeuf and Montel, 1994), including those carried out on rock assemblages of the Araçuaí orogen (Melo et al., 2017a; Richter et al., 2016). Accordingly, garnet and cordierite crystals of the studied neosomes are interpreted as a product of partial melting reactions that consumed biotite, quartz, plagioclase and sillimanite at granulite facies conditions, and produced peritectic phases (garnet and/or cordierite), according to the following reaction by Otamendi and Patiño Douce (2001):

$$Bt + Pl + Qtz + Sill = Grt + Crd + Ilm + Kfs + melt$$

In the studied neosomes, cordierite is the most abundant peritectic mafic mineral formed in equilibrium with partial melting reactions, during the breakdown of biotite, since it is more stable at pressures lower than 5 kbar (Vielzeuf and Montel, 1994). Unless melt extraction is complete, in-situ crystallizing melt back-reacts with the thermal peak phases (cordierite and garnet) upon cooling. The quartz-feldspathic leucosomes with restitic cordierite and/or garnet indicate that at least part of the melt crystallized in situ and, therefore, a degree of back reaction between restite minerals and the melt took place in the studied neosomes (Ashworth and Brown, 1990; Powell, 1983). Formation of biotite by back reaction with a silica-undersaturated melt or local granitic melt can be inferred for the garnet-cordierite neosomes (Fig. 4G and H). Therefore, the retrograde biotite was excluded from the peak P-T paragenesis of the studied phase equilibrium modeling.

Even considering large granitic plutons and heat renew in a contact aureole owing to multiple igneous pulses, it is hard to expect that such a peak temperature range (750–850 °C) can be sustained for more than a few hundred meters from pluton edges (Bucher and Grapes, 2011). However, widespread garnet-cordierite neosomes hosted by granitic migmatites similar to the studied rocks occur for many kilometers far from the Medina granites, as well as far from other G5 batholiths and minor intrusions (*cf.* De Campos et al., 2016; Gradim et al., 2014; Pedrosa-Soares et al., 2011; and references therein). Indeed, this suggest a thermal process more complex than a simple contact metamorphism.

7.4. A model for the post-collisional thermal event in the Araçuaí orogen

The post-collisional thermal event responsible for the generation of a myriad of G5 intrusions has been reported since the first systematic studies on the Araçuaí orogenic granites, being generally related to asthenosphere ascent during the gravitational collapse of the orogen (*cf.* De Campos et al., 2004, 2016; Gradim et al., 2014; Pedrosa-Soares et al., 2001, 2011; Pedrosa-Soares and Wiedemann-Leonardos, 2000). The late orogenic extensional tectonics (Alkmim et al., 2006, 2017; Marshak et al., 2006) was accompanied by low-P – high-T metamorphism (Peixoto et al., 2018; and references therein). Mafic cores and enclaves within G5 granitic plutons, as well as single gabbro-noritic G5 intrusions, together with geochemical and isotopic signatures, have been quoted as the main evidences for mantle involvement in the post-collisional thermal event (*cf.* De Campos et al., 2004, 2016; Pedrosa-Soares et al., 2011; and references therein).

We present the first quantitative study relating G5 granites and coeval thermal effects, involving significant partial melting on their host granitic rocks. Our U—Pb data and lithochemical signatures clearly demonstrate that the ca. 500 Ma Medina granites represent an oxidized A1-type magmatism geochemically related to an OIB-type source, implying in the involvement of a rising mantle plume during the post-collisional stage in the ensialic sector of the Araçuaí orogen. Besides the expected contact metamorphism, our field and analytical data, together with descriptions found in the literature previously quoted, also suggest that partial melting took place in country rocks far from the G5 intrusions. The presented U—Pb data and phase equilibrium modeling estimates from the host granitic migmatites of the Medina batholith constrain a post-collisional anatectic episode around 500 Ma at P-T conditions of 750 to 840 °C at 2.4 to 3.5 kbar. This reinforces a model involving a rising mantle plume, already suggested by the Medina batholith signature. Such a mantle plume provided and enhanced enough heat to induce anatectic melts by the increasing in the geothermal gradient, at the same epoch of the Medina batholith emplacement. The combined zircon and monazite U—Pb geochronology bracketed the late orogenic thermal event in the range of ca. 510–490 Ma, involving the coeval emplacement of A1-type plutons, and regional anatexis on country rocks and fluid circulation.

Our model suggests that, following the fading of collisional convergent stresses, the combination of gravitational collapse, decompression along extensional zones and ascent of a mantle plume, representing a large sub-crustal heat source, triggered and sustained a late orogenic thermal event in the ensialic sector of the Araçuaí orogen (Fig. 15).

8. Conclusions

We present field and analytical studies that, together with a thorough compilation of the literature, support the following conclusions:

1. U—Pb zircon and monazite dating constrain the late orogenic magmatism represented by the Medina granites around 500 Ma.
2. The Medina batholith comprises oxidized A1-type granites, representing H_2O-rich crustal melts, and abundant melanocratic to mesocratic enclaves displaying solid evidence of magma mingling and mixing with a basic magma component.
3. Sources of the A1-type Medina granites are geochemically related to those of magmas derived from oceanic-island basalts (OIB), emplaced in continental rifts or in late orogenic intra-plate settings.
4. The evidence described in this work indicates an episode of post-collisional anatexis in the ensialic sector of the Araçuaí orogen. In this late thermal event, foliated sillimanite-garnet-biotite metagranites, ascribed to the collisional G2 supersuite, melted to produce anhydrous, peraluminous granitic melts crystallized as post-kinematic, non-foliated, garnet-cordierite neosomes. These neosomes, dated around 500 Ma, are found either very close to or many kilometers apart from the Medina granite edges, suggesting more complex thermal process than a simple contact metamorphism of high temperature.
5. The studied garnet-cordierite neosomes (ca. 500 Ma), related to the redefined G3 supersuite (545–500 Ma; Table 1), are coeval with the G5 plutonism and, in fact, represent a post-collisional thermal event that can be of much more regional importance than suggested in the current literature.
6. The phase equilibrium modeling using bulk composition of a garnet-cordierite neosome, dated at ca. 500 Ma, indicates that the inferred thermal peak mineral assemblage (Pl-Kfs-Grt-Crd-Ilm-Qz-Sil) equilibrated at 750–840 °C and 2.4–3.5 kbar. The thermal peak estimates are in agreement with cordierite and garnet formation via an incongruent melting reaction that consumed biotite and sillimanite. Such P-T condition, that controlled the generation of a very significant amount of widespread post-collisional garnet-cordierite neosomes formed from the partial melting of collisional G2 metagranitic rocks, requires a heat source greater than the Medina batholith itself.
7. Therefore, our detailed characterization of the Medina A1-type granites and their host rocks allows us to suggest a model involving the rising of a mantle plume related to gravitational collapse in the ensialic sector of the Araçuaí orogen (Fig. 15).

Acknowledgements

The authors acknowledge financial support provided by Brazilian research and development agencies (CNPq, CAPES and CODEMIG); and the Microscopy and Microanalysis Laboratory (LMIc) of the Universidade Federal de Ouro Preto, a member of the Microscopy and Microanalysis Network of Minas Gerais State/Brazil/FAPEMIG, for the

mineral chemistry analyses. A.C. Pedrosa-Soares, C. Lana, I. Dussin and G. Queiroga, as fellows of the Brazilian Research Council (CNPq), acknowledge the CNPq for their grants. Our gratitude to Professor Xian-Hua Li, Editor-in-Chief of Lithos, and two anonymous reviewers for their suggestions, comments and corrections that greatly help us to improve this paper.

Appendix A. Supplementary data

Supplementary data to this article can be found online at https://doi.org/10.1016/j.lithos.2018.09.009.

References

Alkmim, F.F., Marshak, S., Pedrosa-Soares, A.C., Peres, G.G., Cruz, S.C.P., Whittington, A., 2006. Kinematic evolution of the Araçuaí-West Congo orogen in Brazil and Africa: nutcracker tectonics during the Neoproterozoic assembly of Gondwana. Precambrian Res. 149, 43–64.

Alkmim, F., Kuchenbecker, M., Reis, H., Pedrosa-Soares, A.C., 2017. The Araçuaí Belt. In: Heilbron, M., Cordani, U.G., Alkmim, F.F. (Eds.), São Francisco Craton, Eastern Brazil: Tectonic Genealogy of a Miniature Continent, first ed. Springer International Publishing, Brazil, pp. 255–276.

Ashworth, J.R., Brown, M., 1990. High-Temperature Metamorphism and Crustal Anatexis. second ed. Springer, Netherlands.

Belém, J., 2014. Geoquímica, geocronologia e contexto geotectônico do magmatismo máfico associado ao feixe de fraturas Colatina, Estado do Espírito Santo. Instituto de Geociências, Universidade Federal de Minas Gerais, Belo Horizonte (Phd Thesis, 134 pp.).

Bonin, B., 2007. A-type granites and related rocks: evolution of a concept, problems and prospects. Lithos 97, 1–29.

Boynton, W.V., 1984. Geochemistry of the rare earth elements: meteorites studies. In: Henderson, P. (Ed.), Rare Earth Element Geochemistry. Elsevier, pp. 63–114.

Bucher, K., Grapes, R., 2011. Petrogenesis of Metamorphic Rocks. eighth ed. Springer-Verlag, Berlin Heidelberg.

Cabral, A.R., Tupinambá, M., Zeh, A., Lehmann, B., Wiedenbeck, M., Brauns, M., Kwitko-Ribeiro, R., 2017. Platiniferous gold–tourmaline aggregates in the gold–palladium belt of Minas Gerais, Brazil: implications for regional boron metasomatism. Mineral. Petrol. 111, 807–819.

Cordani, U.G., Brito-Neves, B.B., D'Agrella, M.S., Trindade, R.I.F., 2003. Tearing-up Rodinia: the Neoproterozoic paleogeography of South American cratonic fragments. Terra Nova 15, 343–349.

Dahlquist, J.A., Alasino, P.H., Eby, G.N., Galindo, C., Casquet, C., 2010. Fault controlled Carboniferous A-type magmatism in the proto-Andean foreland (Sierras Pampeanas, Argentina): geochemical constraints and petrogenesis. Lithos 115, 65–81.

Dall'Agnol, R., Oliveira, D.C., 2007. Oxidized, magnetite-series, rapakivi-type granites of Carajás, Brazil: implications for classification and petrogenesis of A-type granites. Lithos 93, 215–233.

Dall'Agnol, R., Scaillet, B., Pichavant, M., 1999. An experimental study of a Lower Proterozoic A-type granite from the Eastern Amazonian craton, Brazil. J. Petrol. 40, 1673–1698.

Dall'Agnol, R., Teixeira, N.P., Rämö, O.T., Moura, C.A.V., Macambira, M.J.B., Oliveira, D.C., 2005. Petrogenesis of the Paleoproterozoic, rapakivi, A-type granites of the Archean Carajás Metallogenic Province, Brazil. Lithos 80, 101–129.

De Campos, C.P., Medeiros, S.R., Mendes, J.C., Pedrosa-Soares, A.C., Dussin, I., Ludka, I.P., Dantas, E.L., 2016. Cambro-Ordovician magmatism in the Araçuaí Belt (SE Brazil): snapshots from a post-collisional event. J. S. Am. Earth Sci. 68, 248–268.

De Campos, C.P., Mendes, J.C., Ludka, I.P., Medeiros, S.R., Moura, J.C., Wallfass, C., 2004. A review of the Brasiliano magmatism in southern Espírito Santo, Brazil, with emphasis on post-collisional magmatism. J. Virtual Explor. 17, 1–39.

De Capitani, C., Petrakakis, K., 2010. The computation of equilibrium assemblage diagrams with Theriak/Domino software. Am. Mineral. 95, 1006–1016.

Deer, W.A., Howie, R.A., Zussman, J., 1992. An Introduction to the Rock Forming Minerals. Second Longman Editions. Longman, London, p. 696.

Degler, R., Pedrosa-Soares, A.C., Dussin, I., Queiroga, G., Schulz, B., 2017. Contrasting provenance and timing of metamorphism from paragneisses of the Araçuaí-Ribeira orogenic system, Brazil: Hints for Western Gondwana assembly. Gondwana Res. 51, 30–50.

Deluca, C., Pedrosa-Soares, A.C., Dussin, I., Queiroga, G., Lana, C., 2018. Petrogênese e evolução tardia de granitos da região de Coronel Murta - Itinga (MG), Orógeno Araçuaí Setentrional. In: Palermo, N., Araújo, H.I., Machado, F.B., Corval, A., Valente, S.C., Dal'Bó, P.F. (Eds.), Anais do 49° Congresso Brasileiro de Geologia. SBG, Rio de Janeiro, p. 1696.

Deng, X., Zhao, T., Peng, T., 2016. Age and geochemistry of the early Mesoproterozoic A-type granites in the southern margin of the North China craton: constraints on their petrogenesis and tectonic implications. Precambrian Res. 283, 68–88.

Eby, G.N., 1990. The A-type granitoids: a review of their occurrence and chemical characteristics and speculations on their petrogenesis. Lithos 26, 115–134.

Eby, G.N., 1992. Chemical subdivision of the A-type granitoids: petrogenetic and tectonic implications. Geology 20, 641–644.

Fernandes, M.L.S., 1991. Geologia, petrografia e geoquímica de rochas granitoides da região de Pedra Azul, MG. Instituto de Geociências, Universidade Federal do Rio de Janeiro, Rio de Janeiro (MSc Dissertation, 191 pp.).

Fitzsimons, I.C.W., 1996. Metapelitic migmatites from Brattstrand Bluffs, East Antarctica—metamorphism, melting and exhumation of the mid crust. J. Petrol. 37, 395–414.

Frost, B.R., Barnes, C.G., Collins,W.J., Arculus, R.J., Ellis, D.J., Frost, C.D., 2001. A geochemical classification for granitic rocks. J. Petrol. 42, 2033–2048.

Frost, C.D., Frost, B.R., 1997. High-K, iron-enriched rapakivi-type granites: the tholeiite connection. Geology 25, 647–650.

Gonçalves, L., Alkmim, F.F., Pedrosa-Soares, A.C., Dussin, I., Valeriano, C., Lana, C., Tedeschi, M., 2016. Granites of the intracontinental termination of a magmatic arc: an example from the Ediacaran Araçuaí orogen, southeastern Brazil. Gondwana Res. 36, 439–459.

Gonçalves, L., Alkmim, F.F., Pedrosa-Soares, A., Gonçalves, C.C., Vieira, V., 2018. From the plutonic root to the volcanic roof of a continental magmatic arc: a review of the Neoproterozoic Araçuaí orogen, southeastern Brazil. Int. J. Earth Sci. 107, 337–358.

Gonçalves-Dias, T., Caxito, F.A., Pedrosa-Soares, A.C., Stevenson, R., Dussin, I., Silva, L.C., Alkmim, F., Pimentel, M., 2016. Age, provenance and tectonic setting of the high-grade Jequitinhonha complex, Araçuaí orogen, eastern Brazil. Brazilian J. Geol. 46, 199–219.

Gradim, C., Roncato, J., Pedrosa-Soares, A.C., Cordani, U., Dussin, I., Alkmim, F.F., Queiroga, G., Jacobssohn, T., Silva, L.C., Babinski, M., 2014. The hot back-arc zone of the Araçuaí orogen, Eastern Brazil: from sedimentation to granite generation. Brazilian J. Geol. 44, 155–180.

Hanchar, J.M., Watson, E.B., 2003. Zircon saturation thermometry. Rev. Mineral. Geochem. 53, 89–112.

Holland, T.J.B., Powell, R., 2011. An improved and extended internall consistent thermodynamic dataset for phases of petrological interest, involving a new equation of state for solids. J. Metamorph. Geol. 29, 333–383.

Johnson, T.E., White, R.W., Powell, R., 2008. Partial melting of metagreywacke – a calculated mineral equilibria study. J. Metamorph. Geol. 26, 837–853.

King, P.L., Chappell, B.W., Allen, C.M., White, A.J.R., 2001. Are A-type granites the high temperature felsic granites? Evidence from fractionated granites of the Wangrah Suite. Aust. J. Earth Sci. 48, 501–514.

Loiselle, M.C., Wones, D.R., 1979. Characteristics and origin of anorogenic granites. Geol. Soc. Am. Abstr. Programs 11, 468.

Marshak, S., Alkmim, F.F., Whittington, A., Pedrosa-Soares, A.C., 2006. Extensional collapse in the Neoproterozoic Araçuaí orogen, eastern Brazil: a setting for reactivation of asymmetric crenulation cleavage. J. Struct. Geol. 28, 129–147.

de Martins, V.T., Teixeira, W., Noce, C.M., Pedrosa-Soares, A.C., 2004. Sr and Nd Characteristics of Brasiliano/Pan-African Granitoid Plutons of the Araçuaí Orogen, Southeastern Brazil: Tectonic Implications. Gondwana Res. 7, 75–89.

Medeiros, S.R., Wiedemann, C.M., Mendes, J.C., 2000. Post-collisional magmatism in the Araçuaí-Ribeira Mobile belt: geochemical and isotopic study of the Várzea Alegre intrusive complex (VAIC), ES, Brazil. Rev. Bras. Geosci. 1, 30–34.

Melo, M.G., Stevens, G., Lana, C., Pedrosa-Soares, A.C., Frei, D., Alkmim, F.F., Alkmin, L.A., 2017a. Two cryptic anatectic events within a syn-collisional granitoid from the Araçuaí orogen (southeastern Brazil): evidence from the polymetamorphic Carlos Chagas batholith. Lithos 277, 51–71.

Melo, M.G., Lana, C., Stevens, G., Pedrosa-Soares, A.C., Gerdes, A., Alkmin, L.A., Nalini, H.A., Alkmim, F.F., 2017b. Assessing the isotopic evolution of S-type granites of the Carlos Chagas batholith, SE Brazil: clues from U-Pb, Hf isotopes, Ti geothermometry and trace element composition of zircon. Lithos 284-285, 730–750.

Miller, C.F., McDowell, S.M., Mapes, R.W., 2003. Hot and cold granites? Implications of zircon saturation temperatures and preservation of inheritance. Geology 31, 529–532.

Nardi, L.V.S., Bitencourt, M.F., 2009. A-type granitoids in post-collisional settings from southernmost Brazil: their classification and relationship with magmatic series. Can. Mineral. 47, 1493–1504.

Narduzzi, F., Farina, F., Stevens, G., Lana, C., Nalini-Jr, H.A., 2017. Magmatic garnet in the Cordilleran-type Galiléia granitoids of the Araçuaí belt (Brazil): evidence for crystallization in the lower crust. Lithos 283, 82–97.

Nicoli, G., Stevens, G., Moyen, J.F., Frei, D., 2015. Rapid evolution from sediment to anatectic granulite in an Archean continental collision zone: the example of the Bandelierkop Formation metapelites, South marginal Zone, Limpopo Belt, South Africa. J. Metamorph. Geol. 33, 177–202.

Novo, T.A., Pedrosa-Soares, A., Vieira, V.S., Dussin, I., Silva, L.C., 2018. The Rio Doce Group revisited: an Ediacaran arc-related volcano-sedimentary basin, Araçuaí orogen (SE Brazil). J. S. Am. Earth Sci. 85, 345–361.

Otamendi, J.E., Patiño Douce, A.E., 2001. Partial melting of aluminous metagreywackes in the northern Sierra de Comechingones, Central Argentina. J. Petrol. 42, 1751–1772.

Paes V., Raposo F., Pinto, P., Oliveira F. 2010. Projeto Jequitinhonha, Estados de Minas Gerais e Bahia: texto explicativo. Geologia e Recursos Minerais das Folhas Comercinho, Jequitinhonha, Almenara, Itaobim, Joaíma e Rio do Prado. Programa Geologia do Brasil, CPRM, Belo Horizonte.

Patiño Douce, A.E., Beard, J.S., 1996. Effects of P, $f(O_2)$ and Mg/Fe ratio on dehydration melting of model metagreywackes. J. Petrol. 37, 999–1024.

Pearce, J., Harris, N.B.W., Tindle, A.G., 1984. Trace element diagrams for the tectonic interpretation of granitic rocks. J. Petrol. 25, 956–983.

Pedrosa-Soares A.C., Alkmim F.F., Tack L., Noce C.M., Babinski M., Silva L.C., Martins-Neto M.A., 2008. Similarities and Differences between the Brazilian and African Counterparts of the Neoproterozoic Aracuai-West Congo Orogeny, in: Pankhurst, J.R., Trouw, R.A.J., Brito Neves, B.B., De Wit, M.J. (Eds.), West Gondwana: Pre-Cenozoic Correlations across the South Atlantic Region. Geological Society, London, pp. 153–172.

Pedrosa-Soares, A.C., De Campos, C.P., Noce, C., Silva, L.C., Novo, T., Roncato, J., Medeiros, S., Castañeda, C., Queiroga, G., Dantas, E., Dussin, I., Alkmim, F., 2011. Late Neoproterozoic–Cambrian granitic magmatism in the Araçuaí orogen (Brazil), the Eastern Brazilian Pegmatite Province and related mineral resources. Geol. Soc. Lond. Spec. Publ. 350, 25–51.

Pedrosa-Soares, A.C., Noce, C.M., Wiedemann, C.M., Pinto, C.P., 2001. The Aracuai-West-Congo Orogen in Brazil: an overview of a confined orogen formed during Gondwanaland assembly. Precambrian Res. 110, 307–323.

Pedrosa-Soares, A.C., Wiedemann-Leonardos, C.M., 2000. Evolution of the Araçuaí Belt and its Connection to the Ribeira Belt, Eastern Brazil. In: Cordani, U.G., Milani, E.J., Thomas Filho, A., Campos, D.A. (Eds.), Tectonic Evolution of South America. CPRM, Rio de Janeiro, pp. 265–285.

Pedrosa-Soares, A.C., Vidal, P., Leonardos, O.H., Brito-Neves, B.B., 1998. Neoproterozoic oceanic remnants in eastern Brazil: further evidence and refutation of an exclusively ensialic evolution for the Araçuaí–West Congo Orogen. Geology 26, 519–522.

Peixoto, E., Pedrosa-Soares, A.C., Alkmim, F.F., Dussin, I.A., 2015. A suture-related accretionary wedge formed in the Neoproterozoic Araçuaí orogen (SE Brazil) during western Gondwanaland assembly. Gondwana Res. 27, 878–896.

Peixoto, E., Alkmim, F.F., Pedrosa-Soares, A.C., Lana, C., Chaves, A.O., 2018. Metamorphic record of collision and colapse in the Ediacaran-Cambrian Araçuaí orogeny, SE-Brazil: Insights from P-T pesudosections and monazite dating. J. Metamorph. Geol. 36, 147–172.

Powell, R., 1983. Processes in granulite facies metamorphism. In: Atherton, M.P., Gribble, C.D. (Eds.), Migmatites, Melting and Metamorphism. Shiva, Nantwich, pp. 127–141.

Queiroga, G., Schulz, B., Martins, M., Castro, M.P., Pedrosa-Soares, A.C., Jordt-Evangelista, H., Silva, A.L., 2016. Thermobarometry and electron-microprobe Th-U-Pb monazite dating in garnet metapelites from the Capelinha Formation, Araçuaí orogen, Brazil. REM-Int. Eng. J. 69, 33–44.

Richter, F., Lana, C., Stevens, G., Buick, I., Pedrosa-Soares, A.C., Alkmim, F.F., Cutts, K., 2016. Sedimentation, metamorphism and granite generation in a back-arc region: records from the Ediacaran Nova Venécia complex (Araçuaí Orogen, Southeastern Brazil). Precambrian Res. 272, 78–100.

Stevens, G., Clemens, J.D., Droop, G.T.R., 1997. Melt production during granulite-facies anatexis: experimental data from “primitive” metasedimentary protholiths. Contrib. Mineral. Petrol. 128, 352–370.

Sun, S.S., McDonough, W.F., 1989. Chemical and isotopic systematics of oceanic basalts; implications for mantle composition and processes. In: Saunders, A.D., Norry, M.J. (Eds.), Magmatism in the Ocean Basins. Geological Society of London, pp. 313–345.

Tedeschi, M., Novo, T., Pedrosa-Soares, A.C., Dussin, I., Tassinari, T., Silva, L.C., Gonçalves, L., Alkmim, F.F., Lana, C., Figueiredo, C., Dantas, E., Medeiros, S., De Campos, C., Corrales, F., Heilbron, M., 2016. The Ediacaran Rio Doce magmatic arc revisited (Araçuaí-Ribeira orogenic system, SE Brazil). J. S. Am. Earth Sci. 68, 167–186.

Vallinayagam, G., Kochhar, N., 2011. Petrological Evolution and Emplacement of Siwana and Jalor Ring Complexes of Malani Igneous Suite, Northwestern Peninsular India. In: Ray, J., Sen, G., Ghosh, B. (Eds.), Topics in Igneous Petrology. Springer, Heidelberg, pp. 437–448.

Vavra, G., Schmid, R., Gebauer, D., 1999. Internal morphology, habit and U–Th–Pb microanalysis of amphibolite- to granulite-facies zircons: geochronology of the Ivrea Zone (Southern Alps). Contrib. Mineral. Petrol. 134, 380–404.

Vielzeuf, D., Montel, J.M., 1994. Partial melting of metagreywackes. Part I. Fluid-absent experiments and phase relationships. Contrib. Mineral. Petrol. 117, 375–393.

Watson, E.B., Harrison, T.M., 1983. Zircon saturation revisited temperature and composition effects in a variety of crustal magma types. Earth Planet. Sci. Lett. 64, 295–304.

Whalen, J.B., Currie, K.L., Chappell, B.W., 1987. A-type granites: geochemical characteristics, discrimination and petrogenesis. Contrib. Mineral. Petrol. 95, 407–419.

White, R.W., Powell, R., Holland, T.J.B., 2001. Calculation of partial melting equilibria in the system Na_2O-CaO-K_2O-FeO-MgO-Al_2O_3-SiO_2-H_2O (NCKFMASH). J. Metamorph. Geol. 19, 139.